AD-780 169

SEISMOLOGY AND ACOUSTIC-GRAVITY WAVES

David G. Harkrider

California Institute of Technology

Prepared for:

Air Force Office of Scientific Research
Advanced Research Projects Agency

1973

DISTRIBUTED BY:

NTIS

National Technical Information Service
U. S. DEPARTMENT OF COMMERCE
5285 Port Royal Road, Springfield Va. 22151

UNCLASSIFIED

SECURITY CLASSIFICATION OF THIS PAGE (When Data Entered)

REPORT DOCUMENTATION PAGE

READ INSTRUCTIONS BEFORE COMPLETING FORM

1. REPORT NUMBER: AFOSR - TR - 74 - 0868
2. GOVT ACCESSION NO.
3. RECIPIENT'S CATALOG NO.: AD 780169
4. TITLE (and Subtitle): SEISMOLOGY AND ACOUSTIC-GRAVITY WAVES
5. TYPE OF REPORT & PERIOD COVERED: Final Report 1 Jan. 1973-30 June 1973
6. PERFORMING ORG. REPORT NUMBER
7. AUTHOR(s): David G. Harkrider
8. CONTRACT OR GRANT NUMBER(s): F44620-70-C-0120
9. PERFORMING ORGANIZATION NAME AND ADDRESS: California Institute of Technology, Seismological Laboratory, P.O. Bin 2-Arroyo Annex, Pasadena, Calif. 91109
10. PROGRAM ELEMENT, PROJECT, TASK AREA & WORK UNIT NUMBERS: ARPA Order 846, Program Code 0F10, Program Element Code 62701D
11. CONTROLLING OFFICE NAME AND ADDRESS: AFOSR, 1400 Wilson Blvd. (NPG), Arlington, Virginia 22209
12. REPORT DATE: 1973
13. NUMBER OF PAGES: 104
14. MONITORING AGENCY NAME & ADDRESS (if different from Controlling Office)
15. SECURITY CLASS. (of this report): Unclassified
15a. DECLASSIFICATION/DOWNGRADING SCHEDULE
16. DISTRIBUTION STATEMENT (of this Report): Approved for public release; distribution unlimited
17. DISTRIBUTION STATEMENT (of the abstract entered in Block 20, if different from Report)
18. SUPPLEMENTARY NOTES

Reproduced by NATIONAL TECHNICAL INFORMATION SERVICE U.S. Department of Commerce Springfield VA 22151

19. KEY WORDS (Continue on reverse side if necessary and identify by block number)

Underground explosions
Stochastic inverse applied to surface displacements
Excitation of Rayleigh waves
Excitation of acoustic gravity waves
(Cont'd.)

20. ABSTRACT (Continue on reverse side if necessary and identify by block number)

Previous semi-annual technical reports under this contract have dealt with the generation of acoustic-gravity waves and Rayleigh waves by explosive sources. In particular, research was done and reported in the following areas:

a. Theoretical acoustic-gravity waves generated by surface displacements associated with models of contained underground explosions.

b. Theoretical acoustic-gravity waves and Rayleigh waves generated by underground explosions.

c. Preliminary theoretical determination of M_s versus yield of underground

DD FORM 1 JAN 73 1473 EDITION OF 1 NOV 65 IS OBSOLETE

UNCLASSIFIED

SECURITY CLASSIFICATION OF THIS PAGE (When Data Entered)

AFOSR - TR - 74 - 0862

AD780169

California Institute of Technology
Division of Geological and Planetary Sciences
Seismological Laboratory
Pasadena, California 91109

FINAL REPORT

1 January 1973 - 30 June 1973

DDC
RECEIVED
JUN 14 1974
C

ARPA Order No:	846
Program Code:	OFIO
Name of Contractor:	California Institute of Technology
Effective Date of Contract:	1 July 1970
Contract Expiration Date:	30 June 1973
Amount of Contract	$52,749
Contract Number:	F44620-70-C-0120
Principal Investigator and Phone Number:	David G. Harkrider (213) 795-8806
Program Manager and Phone Number:	William J. Best (202) 694-5456
Short Title of Work:	Seismology and Acoustic-Gravity Waves

AIR FORCE OFFICE OF SCIENTIFIC RESEARCH (AFSC)
NOTICE OF TRANSMITTAL TO DDC
This technical report has been reviewed and is approved for public release IAW AFR 190-12 (7b).
Distribution is unlimited.
D. W. TAYLOR
Technical Information Officer

Reproduced by
NATIONAL TECHNICAL
INFORMATION SERVICE
U S Department of Commerce
Springfield VA 22151

Sponsored by
Advanced Research Projects Agency
ARPA Order No. 846

ib

19. Key Words (Cont'd)
Review of acoustic gravity wave source theory
Dislocation inversion of 1971 San Fernando earthquake

20. Abstract (Continued)

explosions

d. Theoretical and observed distance corrections for Rayleigh wave magnitudes

e. Seismic source descriptions of underground explosions and a depth discriminate

f. Radiation and attenuation of Rayleigh waves from the southeastern Missouri earthquake of October 21, 1965.

g. Theoretical effect of yield and burst height of atmospheric explosions of Rayleigh wave amplitudes

h. Development of the stochastic inverse as applied to static dislocation problems.

i. A static dislocation model of 1964 Alaska earthquake

CONTENTS

I. Summary

II. Source and linear propagation theory of acoustic-gravity waves

III. A static dislocation model of the 1971 San Fernando earthquake

I. Summary

Previous semi-annual technical reports under this contract have dealt with the generation of acoustic-gravity waves and Rayleigh waves by explosive sources. In particular, research was done and reported in the following areas:

a. Theoretical acoustic-gravity waves generated by surface displacements associated with models of contained underground explosions

b. Theoretical acoustic-gravity waves and Rayleigh waves generated by underground explosions

c. Preliminary theoretical determination of M_s versus yield of underground explosions

d. Theoretical and observed distance corrections for Rayleigh wave magnitudes

e. Seismic source descriptions of underground explosions and a depth discriminate

f. Radiation and attenuation of Rayleigh waves from the southeastern Missouri earthquake of October 21, 1965.

g. Theoretical effect of yield and burst height of atmospheric explosions on Rayleigh wave amplitudes

h. Development of the stochastic inverse as applied to static dislocation problems

i. A static dislocation model of 1964 Alaska earthquake

Section II of the final report is a review and evaluation of source and linear propagation theory of acoustic-gravity waves. The discussion is

limited to the literature involving acoustic-gravity waves which travel in the lower atmosphere and to solutions not involving finite difference and finite element techniques.

In Section III, the static displacement data obtained for the 1971 San Fernando, California, earthquake are used to try to determine the faulting mechanism for that event. The forward problem is solved using a three-dimensional dislocation theory applicable to a homogeneous half-space. The dislocation model calculated to optimally fit the observed data indicate a large degree of spatial variability of dislocation along the assumed fault surfaces. Part of the data set used in the inversion is that obtained by converting changes in the gravity field into changes in elevation associated with the earthquake.

SOURCE AND LINEAR PROPAGATION THEORY OF ACOUSTIC-GRAVITY WAVES

This discussion is limited to the literature involving acoustic-gravity pressure waves which travel in the lower atmosphere and to solutions not involving finite difference techniques such as Green and Whitaker (1968), Potemra (1965), etc.

One of the earliest contributions to the theoretical analysis of infrasonic wave trains produced by ground level explosions in an atmosphere was that by Pekeris (1948). This was closely followed by Scorer (1950). Pekeris (1948) formulated the problem of a surface source which injects vertically a volume of gas into the atmosphere. He obtained solutions for two atmospheric models in terms of a Fourier and a Fourier-Bessel integrals. In one model the atmosphere was isothermal and in the other the atmosphere consisted of a troposphere having a constant lapse rate and an isothermal stratosphere with continuity of temperature at the tropopause. The roots of the resulting dispersion relations were discussed but no attempt was made to calculate the predicted wave train. Scorer (1950) using a slightly different, but equivalent, formulation calculated the pressure pulse at various ranges for the two layer model of Pekeris. As pointed out by Hunt, Palmer and Penny (1960), Scorer sued a modified stationary phase technique valid for very large distances which was unlikely to give a good representation of experimental observations.

Yamamoto (1957) calculated the fundamental mode of two-layer and four-layer atmospheres. Yamamoto's calculations were motivated by his observation that the pulses from large explosions begin with long period waves with the later arrivals in the dispersed signal having periods as short as 0.2 min. Since Yamamoto could not obtain a cutoff period of less than 1.5 minutes for a two layer model with the upper layer colder than the lower, he concluded that the observed microbarograms could not be explained with the two-layer. For a four-layer model with the top layer being the warmest, he found fundamental mode solutions with periods down to 0.5 minutes and a group velocity curve with a minimum. His study did not include the pulse calculations.

Hunt, et al (1960), using the Pekeris and Scorer model and a two isothermal layer and a three isothermal layer model, investigated the character of the acoustic-gravity modes and synthesized their portion of the pressure pulse produced by explosions on the ground. Their discussion of the influence of vertical temperature structure on the character of these modes is probably the most physically instructive analysis in the literature. This is true in spite of the fact that in adopting Scorer's formulation to the isothermal layer and models, they used the incorrect boundary condition between layers of continuity of the perturbed pressure evaluated at the ambient position of the interface instead of at the perturbed position (Hines, 1960). To the first order, the two boundary conditions are equivalent if there is no discontinuity in ambient density across the interface as in Pekeris and Scorer. This error only effects Hunt et al's quantitative results. Their qualitative conclusions are still valid.

For the two isothermal layer atmosphere Hunt et al found that as long as the stratosphere half-space was colder than troposphere layers, there was only one mode which terminated with a high frequency cutoff. The velocity of this mode varied between the two layer velocities and was equal to the stratosphere velocity at cutoff. This was also predicted by Pekeris and Scorer. When the temperature of both layers is the same and the model represents an isothermal half-space, there is again only one mode. This is the Lamb mode which is trapped at the rigid surface with a vertical particle velocity equal to zero everywhere and travels at the acoustic velocity of the half-space. Pekeris obtained a ficticious second mode for the half-space which corresponds to the surface wave for a half-space with only a free-surface boundary at its top. Once the top layer was made warmer, they found an infinite number of modes with no high-frequency cutoff for any of the modes and a low frequency cutoff for all the modes except the first. The analyses of the roots of this simple model demonstrated that if there is a temperature minimum, i.e. sound channel, in the atmosphere, then there will be no high frequency cutoff. This corrected the erroneous "conjecture of Pekeris (1948) that all stratified atmospheres having a temperature minimum would exhibit a high-frequency cutoff. " This model also shows that the higher modes will have a low frequency cutoff.

Weston (1961) using a Green's function approach obtained the solution for a pressure pulse produced by explosions not only on the ground, but at various heights in the atmosphere of spherical earth. In the formulation he shows how the eigenfunction for a plane stratified

model can be corrected for a spherical cap spreading to represent the pulse propagating over a spherical earth. The pulse was synthesized for three models, one the Scorer model and the other two were variations of the stratosphere minimum up to a slightly colder than the surface, half-space beginning at 50 km.

Weston (1962) calculated the pressure perturbation as in his earlier paper using a more realistic model of the atmosphere with two temperature ducts and a large temperature gradient in the atmosphere. From his expression he determined there should be a set of modes with velocities less than the velocity of the more extreme temperature minimum in the atmosphere and with periods always greater than the Brunt cut-off period associated with this duct. These modes later called gravity modes were missed by Hunt et al (1960). Since the calculated pulses indicated that their amplitude decrease drastically with the calculated pulses indicated that their amplitude decrease drastically with increasing burst height which was in direct conflict with later investigations, Pierce, Posey and Iliff (1971) concluded that there was a coding error in the computation of Weston's wave forms. Other evidence for this is that the fundamental and higher acoustic-gravity modes of his calculations had a high-frequency cut-off, and according to previous and later investigations, these modes should not have a cut-off for a model with a temperature duct.

In order to evaluate the radial or vertical eigenfunctions and eigenvalues, Weston used numerical integration over the vertical

distribution of temperature. Press and Harkrider (1962), Pfeffer (1962), and Pffeffer and Zarichny (1962, 1963) formulated the eigenvalue problem in terms of a multilayer model of the vertical temperature structure. Yamomoto (1957) and Hunt et al also used an isothermal layer representation; but in the multilayer approach, the layer solutions are combined in a layer matrix such that the multiplication of two contiguous layer matrices satisfies the boundary conditions between the layers. This approach is particularly suited for a computer and does not require the investigators to limit themselves to only a few layers as in Yamomoto and Hunt et al. In the multilayer investigations phase and group velocity dispersion curves and vertical pressure distributions were numerically evaluated in terms of the different models of atmospheric structure. The results of Press and Harkrider (1962) and Pfeffer and Zarichny (1962) differed somewhat because the latter authors terminated their atmosphere model at a lower altitude. Later work with a more complete model by Pfiffer and Zarichny (1963) gives results which agree with those of Press and Harkrider and contain a wider variety of atmospheric models. The multilayer investigations found the same set of modes, generally referred to as acoustic modes which have no high frequency cutoff as found in the simple models of Hunt et al and the gravity modes found by Weston (1962). Press and Harkrider found that the sequence of maximums or plateaus in group velocity formed by the set of acoustic modes and the first two gravity modes is sensitive to the properties of the lower 50 km of the atmosphere. Pfeffer and Zarichny (1963) verified this and indicated that the sequence of plateaus for the higher acoustic modes approach the sound velocity of the lower wave guide as frequency increases.

In addition, the phase and group velocities of the acoustic modes were found to approach the lowest velocity in the atmosphere at the high frequency limit, Press and Harkrider (1962). In most models this is the upper guide at 85 km; therefore the acoustic group velocity minimums, which are controlled by the phase-velocity high frequency asymptote, were sensitive in these models to the atmosphere above 50 km.

While advances were being made in the evaluation and understanding of the atmospheric wave guides, theoretical investigations were being done on modeling explosive sources. Hunt et al (1960), Weston (1961, 1962), Dikii (1962), Pierce (1963), Harkrider (1964), van Halsteyn (1965, I & II), all incorporated a point source in their models for calculations. This Green's function source was expressed in analytic form in the frequency domain for an isothermal region by Dikii (1962) and Pierce (1963). Using a different notation for this source Row (1967) pointed out that the waves emitted by this source in an isothermal region were dispersive and anisotropic, i.e. their velocity was a function of frequency and take-off angle from the vertical. Tolstoy (1963) made the same observation using a different approach.

Harkrider (1964), using an integral representation of the frequency domain expression for the Dikii (1962) and Pierce (1963) point source, synthesized barograms for comparison with observed waves from thermonuclear explosions. The agreement was satisfactory but showed some disturbing differences:

1) The suppression of high frequencies with increasing yield was much more extreme than for that observed expecially for yields above 10 MT.

2) For theoretical barograms in the yield, W, range of 1 to 5 MT, the overpressure varied as $W^{.9}$. For larger yields the amplitude was approximately proportional to $W^{.6}$. The latter differed considerably from the expected direct proportionality to yield, $W^{1.0}$.

3) In increasing the altitude from 2 to 17 km altitude, the theoretical barograms showed an increase in amplitude by about a factor of 6.

Pierce (1965) demonstrated that the pressure scales for the synthetic barograms in Harkrider (1964), were in error due to the omission of a factor used in scaling source functions from one altitude to another. As Pierce pointed out, the corrected effect of increasing source altitude on the amplitudes of the early arriving signal is slight at moderate heights and eventually at great altitudes the signal pressure decreases with increasing source height as one would expect. The net decrease form 2 to 17 km altitude is on the order of 30%.

In addition to comparison with actual events Harkrider (1964), used the source excitation to verify the effects of various portions of the wave guide as postulated by Press and Harkrider (1962), and Pfeffer and Zarichny (1963).

The models discussed above did not include the effect of wind structure. Weston and van Hulsteyn (1962), showed that the linearized equations of hydrodynamics are still separable if the winds are horizontal and vary in direction and magnitude only with altitude. Pridmore-Brown (1962), also derived the generalized equations for sound propagation in an atmosphere with arbitrary sound-speed profile and horizontal wind profile. Weston and van Hulsteyn presented the numerical effect of wind on the phase velocity of one mode propagating downwind. Pridmore-Brown

included a steady state point source.

Pierce (1965) extended the theories of Weston and van Hulsteyn and of Pridmore-Brown to the propagation of infrasonic waves from an idealized point source with an arbitrary time variation. Pierce pointed out that the approximations given by Pridmore-Brown imply that the phase and group velocity direction are the same and point radially from the source. Pierce using a perturbation method and one mode showed that in general this is not true. Pierce (1967 a and b) combined his 1965 formulation with the multilayer approximation to explore in greater detail the effects of winds on modal propagation. As one might expect for pure upwind and downwind directions where the source in line with assumed direction of the wind profile, the phase and group velocity are both in this direction and that the primary difference between upwind and downwind propagation on the early arriving portion of the signal would simply be that waves traveling downward travel faster. In addition the maximum difference between phase and group velocity direction occurs for crosswind propagation.

Pierce and Posey (1970) developed a barogram synthesis program using the multilayer approximation to a temperature and wind stratified atmosphere. In order to facilitate computation of the effect of wind on the pressure trains they neglect the perturbation between phase and group velocity direction due to crosswinds. They compared the wave form for two wind models with two non-wind models in which the sound speed was equal to sound speed of the wind models increased or decreased by the component of the wind velocity in the direction of propagation. They noted that, even though winds were actually treated in a much more sophisticated manner than simply using this effective velocity, the

results imply that the sophistication had only slight effect on the predicted waveforms. Thus, as long as the wind speed in every layer is much less than the speed of sound for that layer, the major effect of wind is simply to change the effective sound speed profile.

The multilayer approximation and the application of normal modes to atmosphere have received many criticisms and questions concerning their validity. Hines (1965), pointed out that the differential equations derived for acoustic-gravity wave propagation in a continuously stratified atmosphere have coefficients which depend on derivatives with respect to height. Pierce (1966), demonstrated that the approximation is rigorously valid in the limit of small layer thicknesses. Pierce and Posey (1970), expressed the philosophy of the technique very well in that the method is only a numerical integration technique. The atmosphere is not modeled by a multilayer model at the outset, but only use it as a device to evaluate numerical quantities of interest. Any given multilayer atmosphere would most likely give erroneous results for sufficiently short wavelength events. Guidelines for selecting the degree of layering have been discussed by Pierce (1967a), Friedman and Crawford (1968), and Vincent (1969).

Another cause for concern was the method terminating the atmosphere at altitude. Even though the dispersion curves in the frequency domain change character as the altitude increases and the boundary condition is changed, the barograms for a source and receiver in the lower atmosphere are relatively unaffected by the atmosphere conditions below 110 km [Harkrider and Wells (1968), and Pierce and Posey (1970)]. Also affected by the upper boundary conditions is the long period cutoff above which long period waves are no longer trapped in an isothermal half-space.

Since this represents vertical radiation out of the atmosphere, an atmosphere terminated at altitude by a free or rigid surface will no longer have this cutoff and waves of infinite period can be trapped in the atmosphere. Friedman (1966), and Harkirder and Wells (1968), performed numerical experiments which indicated that for the extreme case of infinite period for the near earth surface mode traveling in an atmosphere terminated at altitude by a half-space, the leakage of this mode results in a decay in ampitude of 1/3 after a distance equivalent to almost eight encirclements of the earth. Thus the method of atmosphere termination is relatively unimportant to near surface generated and recorded waveforms.

Two more questions concerning the modeling of the atmosphere were the variation of gravity with height [van Hulsteyn (1965 I & II)] and the neglect of velocity or temperature gradients in the isothermal layering approximation. It was felt by some that the neglect of the gravity variation as in the programs of Pierce and Posey (1970) might be important. This was unlikely though since the results of Press and Harkrider (1962), and Harkrider (1964), were obtained using in each layer a value of gravitational acceleration corresponding to that value appropriate for the layer midpoint altitude above a spherical earth, and these results were in agreement with Pierce.

Strong positive gradients in the altitude range from 106 to 175 km form anomalous regions in the atmosphere where the Brient-Vaisala period is less than the acoustic cutoff period. No matter how fine the layering is made in an attempt to model this reigon, it is theoretically impossible to obtain such a region using isothermal layers. Tolstoy (1967), felt that the presence of this region might yield erroneous predictions

based on the multilayer model. Greenfield and Harkrider (1971), studied the effect of neglecting temperature gradients by replacing these gradients with layers having constant gradients and comparing the results with the multilayer calculations. They concluded that the more realistic linear temperature variation models increased the plateau velocity of the fundamental gravity mode by about 0.3 per cent relative to previous isothermal models and that the greatest effect is due to modeling the atmosphere with a linear temperature variation in the lower 11 km. This was not surprising since in the investigated period range this mode is the modal equivalent of the atmospheric surface wave trapped near the Earth's surface. Comparison of constant gravity models with variable gravity models indicated that the effect is less than that caused by using linear temperature variations instead of isothermal layers.

Even with the inclusion of these effects, the original anomalies between observation and theoretical barograms for large nuclear explosions still existed. A major step in resolving these differences was made by Pierce, Posey and Iliff (1971). Using the energy source formulation of Pierce (1968), they calculated waveforms and compared them with a number of observed waveforms previously exhibited by Harkrider (1964). Their source gave much better agreement in the suppression of high frequencies with increasing yield for yields above 10 MT. Their results predict that the early portion of waveforms received on the ground are nearly proportional to yield and increase slowly with height of burst up to a height of the order of 40 km and then rapidly decrease with further increasing height.

Pierce (1968), points out that all previous sources including his own (Pierce, 1963), were equivalent to mass injection sources. The

basic difference between the mass injection and his energy injection source in the excitation of acoustic-gravity wave is that the height effect of the energy source is controlled by the parcel pressure eigenfunction and not the pressure eigenfunction as for a mass source. Thus according to the single composite mode analyses of Pierce et al. (1971), the mass source should have approximately the same behavior with increasing altitude as the energy source of their paper.

The Pierce et al. differences from Harkrider (1964), were not due to the use of the mass source but in Harkrider's requirement that the pressure wave directly below the source have a specified size and time history. This resulted in unrealistic scaling of the effect of source altitude and yield because of the great difference in source altitude and scale point altitude for large yields. For the larger yields the scale distance below the source was much greater than its altitude.

Actually if Harkrider (1964) had used the scaling technique of van Hulsteyn (1965 I & II), in which the observed pressure pulse is used to calculate an equivalent point source, the only difference between his formulation and Pierce and Posey (1970) would have been in the vertical eigenfunction mentioned earlier.

The concept of composite modes used in Pierce et al. (1971) promises to give physical insight and qualitative prediction on the behavior of complicated systems. Press and Harkrider (1962) noted that the phase velocity versus period curves for a realistic atmospheric profile tend to be arranged such that a single curve of nearly constant phase velocity extending over a wide range of periods may be constructed by the connection of the horizontal segments of a number of individual modal dispersion curves. This composite curve was identified by many authors as the real atmosphere's counterpart of the edge mode predicted by

Lamb (1910) for the isothermal atmosphere model. Similarly Pfeffer and Zarichny (1963) reported that the step-like behavior of the pahse velocity curves thus appears to be due to the interference of two families of normal modes - one family in which the energy propagates in the lower atmosphere (the quais-horizontal modes) and the other in which it travels in the upper atmosphere (the quasi-vertical modes). This has been supported by various numerical experiments (Harkrider and Wells, 1968) as well as by examination of the height profiles of associated with different frequencies and modes (Pffeffer and Zarichny, 1963).

The phenomena of composite modes is especially evident in weakly coupled systems such as the ocean-atmosphere system. Press and Harkrider (1966) and Harkrider and Press (1967) demonstrated that the classical incompressible ocean surface wave with long period asymptote, $\sqrt{gH}$, and short period asymptote, $\sqrt{g\lambda}$, where H and λ are ocean depth and horizontal wave elgnth respectively, is formed by such a composite among the higher order gravity models of the atmosphere.

Some implications of the identification of the atmosphere edge mode were recently explored by Bretherton (1969) and by Garrett (1969a,b). Bretherton showed how the mode's phase velocity may be found to first order in deviations of the sound speed profile from that of an isothermal atmosphere and to first order in the wind velocity while Garrett extended the method to higher orders and thus succeeded in finding the dispersion of the mode. The latter paper by Garrett (1965) gives a detailed discussion of the applications of the theory based on the edge mode to the analysis of empirical waveforms, as well as of the limitations of the theory. In spite of the relative simplicity of the Bretherton-Garrett model, it appears to be adequate for the explanation of the

gross propagation speeds and dispersive characteristics of empirical waveforms, although it does not (at least to the extent which the perturbation series has yet been carried) explain more subtle features such as the inverse dispersion suggested by the data analysis of Donn and Ewing (1962).

In Pierce and Posey (1971), the Bretherton-Garrett model is further developed, the objective being a comprehensive but simple model for theoretical synthesis of transient waveforms recorded at large distances from nuclear explosions. The model developed there would appear to give a relatively simple explanation of (i) the magnitude of the amplitudes of the first few peaks, (ii) the periods between the first few peaks, (iii) the fact that records almost always begin with a positive pressure rise, and (iv) the anomalies in the spatial distribution of recorded peak overpressures that have been reported by Wexler and Mass (1962). (Item (iii) above is unfortunately not widely appreciated due to the fact that noise often obscures the early part of the record and that some of the published records have inadvertently been published with the positive pressure axis extending downwards. Professor Donn admitted to them that this was the case in the paper by Donn and Shaw, (1967).) The first three items are also explained by the more elaborate multimode theories (see, for example, Harkrider, 1964) and they accordingly demonstrate that the edge mode model gives results similar to the multimode calculations of Pierce, Posey and Iliff (1971) for the first few cycles. The advantage of the edge mode model is its simplicity, and this allows an exploration of effects whose consideration may have been prohibitively difficult within the context of existing multimode theories. Such effects include accumulative far field nonlinear

effects, the effects of terrain variations and the effects of horizontal atmospheric variations. In their paper, methods of examining such effects of terrain variations and the effects of horizontal atmospheric variations. In their paper, methods of examining such effects via the edge mode model were outlined, although their detailed analysis was relegated to later studies.

REFERENCES

Bretherton, F., 1969. Lamb waves in a nearly isothermal atmosphere. Q. Jl. R. met. Soc., 95, 754-757.

Dikii, L., 1962. Green's function for weak disturbances in a baroclinic isothermally stratified atmosphere, Dokl. Acad. Sci. USSR, 143, (1), 97-100.

Friedman, J., 1966. Propagation of internal gravity waves in a thermally stratified atmosphere, J. geophys. Res., 71, 1033-1054.

Friedman, J. P. and Crawford, B. W., 1968. Iterative series methods for finding exact solutions for a class of second order differential equations, Acoustic-Gravity Waves in the Atmosphere, T. M. Georges, ed., 349-361, U.S. Govt. Printing Office.

Garrett, C. J. R., 1969a. The fundamental mode of acoustic-gravity wave propagation in the atmosphere, Fluid Mech. Trans. Warsaw, 4, 707-719.

Garrett, C. J. R., 1969b. Atmospheric edge waves, Q. Jl. R. met. Soc., 95, 731-753.

Greenfield, R. J. and Harkrider, D. G., 1971. Acoustic-gravity wave calculations in a layer with a linear temperature variation, Geophys. J. R. astr. Soc., 26, 323-339.

Harkrider, D. G., 1964. Theoretical and observed acoustic-gravity waves from explosive sources in the atmosphere, J. geophys. Res., 69, 5295-5321.

Harkrider, D. G., and Press, F., 1967. The Krakatoa air-sea waves: an example of pulse propagation in coupled systems, Geophys. J. R. astr. Soc., 13, 149-159.

Harkrider, D. G. and Wells, F., 1968. Excitation and dispersion of the atmosphere surface wave, Symposium Proc. Acoustic Gravity Waves in the Atmosphere, 299-313, Environmental Sciences Services Administration, Boulder, Colorado.

Hines, C., 1960. Internal atmospheric gravity waves at ionospheric heights, Can. J. Phys., 38, 1441-1481.

Hines, C., 1965. Atmospheric gravity waves: a new toy for the wave theorist, Radio Sci., 69D, 375-380.

Hunt, J., Palmer, R. and Penney, W., 1960. Atmospheric waves caused by large explosions, Phil. Trans. R. Soc. London, A252, 275-315.

Pekeris, C., 1948. The propagation of a pulse in the atmosphere, II, Phys. Rev., 73, 145-154.

Pfeffer, R., 1962. A multi-layer model for the study of acoustic-gravity wave propagation in the Earth's atmosphere, J. atmos. Sci., 19, 251-255.

Pfeffer, R. L., and Zarichny, J., 1962. Acoustic gravity wave propagation from nuclear explosions in the earth's atmosphere, J. atmos. Sci., 19, 256-263.

Pfeffer, R. & Zarichny, J., 1963. Acoustic-gravity wave propagation in an atmosphere with two sound channels, Geofis. pura appl., 55, 175-179.

Pierce, A., 1963. Propagation of acoustic-gravity waves from a small source above the ground in an isothermal atmosphere, J. acoust. Soc. Am., 35, 1798-1807.

Pierce, A., 1965. Propagation of acoustic-gravity waves in a temperature- and wind-stratified atmosphere, J. acoust. Soc. Am., 37, 218-227.

Pierce, A., 1965. Comments on paper by David G. Harkrider, Theoretical and observed acoustiv-gravity waves from explosive sources in the atmosphere, J. geophys. Res., 70, 2463-2464.

Pierce, A., 1966. Justification of the use of multiple isothermal layers as an approximation to the real atmosphere for acoustic-gravity wave propagation, Radio Sci., 1, 265-267.

Pierce, A., 1967a. The multilayer approximation for infrasonic wave propagation in a temperature-and-wind-stratified atmosphere, J. Computational Phys., 1, 343-366.

Pierce, A. D., 1967b. Guided infrasonic modes in a temperature-and-wind-stratified atmosphere, J. acoust. Soc. Am., 41, 597-611.

Pierce, A. D., 1968. Theoretical source models for the generation of acoustic-gravity waves by nuclear explosions, Acoustic-Gravity Waves in the Atmosphere, T. M. Georges, ed., 9-24, U.S. Gov. Printing Office.

Pierce, A. D., & Posey, J. W., 1970. Theoretical predictions of acoustic-gravity pressure waveforms generated by large explosions in the atmosphere, Air Force Cambridge Research Laboratories Report AFCRL-70-134, 312 pp.

Pierce, A. D., & Posey, J. W., 1971. Theory of the excitation and propagation of Lamb's atmospheric edge mode from nuclear explosions, Geophys. J. R. astr. Soc., 26, 341-368.

Pierce, A. D., Posey, J. W. & Iliff, E. F., 1971. Variation of nuclear generated acoustic-gravity waveforms with burst height and with energy yield, J. geophys. Res., 76, 5025-5042.

Potemra, T., 1965. Acoustic-gravity waves in the atmosphere, Stanford Electronics Lab. Tech. Repot. 110, SU-SEL-65-097, Stanford, California.

Press, F. & Harkrider, D., 1962. Propagation of acoustic-gravity waves in the atmosphere, J. geophys. Res., 67, 3889-3908.

Press, F. & Harkrider, D. G., 1966. Air-sea waves from the explosion of Krakatoa, Science, 154, 1325-1327.

Pridmore-Brown, D., 1962. Sound propagation in a temperature-and-wind-stratified atmosphere, J. acoust. Soc. Am., 34, 438-443.

Row, R. V., 1967. Acoustic-gravity waves in the upper atmosphere due to a nuclear detonation and an earthquake, J. geophys. Res., 73, 1599-1610.

Scorer, R., 1950. The dispersion of a pressure pulse in the atmosphere, Proc. R. Soc. Lond., A201, 137-157.

Tolstoy, I., 1963. The theory of waves in stratified fluids including the effects of gravity and rotation, Rev. Mod. Phys., 35, 207-230.

Tolstoy, I., 1967. Long period gravity waves in the atmosphere, J. geophys. Res., 72, 4605-4622.

Van Hulsteyn, D. B., 1965. The atmospheric pressure wave generated by a nuclear explosion, parts I & II, J. geophys. Res., 70, 257-278.

Vincent, R. A., 1969. A criterion for the use of the multi-layer approximation in the study of acoustic-gravity wave propagation, J. geophys. Res., 74, 2996-3001.

Weston, V. H., 1961. The pressure pulse produced by a large explosion in the atmosphere, Can. J. Phys., 39, 993-1009.

Weston, V. H., 1962. The pressure pulse produced by a large explosion in the atmosphere, part II, Can. J. Phys., 40, 431-445.

Weston, V. H. & Van Hulsteyn, D., 1962. The effect of winds on the gravity wave, Can. J. Phys., 40, 797-804.

Yamamoto, R., 1957. A dynamical theory of the microbarographic oscillations produced by the explosions of hydrogen bombs, J. met. Soc. Japan, 35, 288-296.

III. Static Dislocation of the 1971 San Fernando Earthquake

This section is Chapter IV of Ralph Wilson Alewine, III's Thesis (1974) titled "Application of Linear Inversion Theory Toward the Estimation of Seismic Source Parameters. References and details cited in this section can be found in the Thesis. This Thesis has been submitted and successfully defended as partial fulfillment of the requirements of the Degree of Doctor of Philosophy at the California Institute of Technology, Pasadena, California.

Chapter 4

A Static Dislocation Model of the 1971 San Fernando Earthquake

4.1 Introduction.

On February 9, 1971, a local magnitude 6.4 earthquake was initiated below the San Gabriel Mountains north of the San Fernando Valley, California. The surface ruptures from this event occurred some 13-15 km to the south of the epicenter along the Santa Susana-Sierra Madre fault zone which forms the frontal system of the southern boundary of the San Gabriel Mountains. The behavior and pattern of the faulting that occurred during this earthquake exactly repeated and further developed the older, already recognized geologic features--faulting and uplift--of the southern boundary of the San Gabriel Mountains which began in mid-Pleistocene time (Oakeshott, 1958). The stratigraphy and geologic structure of this area have been recently described by Wentworth and Yerkes (1971) and by Proctor *et al.* (1972).

In this chapter, we will not dwell on the geologic setting of the area since it is covered in some detail by the above references; rather, we will propose a fault model, the geometry of which we think to be most consistent with all the geological and geophysical observations that

have been made concerning this earthquake. These observations include the focal mechanism of the main shock, the mechanism and spatial distribution of the aftershock sequence, and the geologic character of the surface faulting. As in the previous chapter, once we have fixed the fault model geometry we will then use the static displacement data available to us along a profile bisecting the surface trace of the fault to determine the static dislocation function for our fault model which is most consistent with this data. Features of this calculated static dislocation model will then be examined for its resolvability, and implications of the model with its associated stresses and strains will then be discussed. Let us look first at the geological and geophysical observations that will constrain our fault model geometry.

4.2 Fault Model Constraints.

Main Shock Focal Mechanism. Unlike the 1964 Alaska earthquake, there seems to be no controversy of the choice of fault planes derived from the first motion studies of the 1971 San Fernando earthquake. The natural ambiguity in the choice of fault planes (assuming a double couple mechanism) is essentially removed by the geometric relation of the determined hypocenter and the observed thrust fault surface ruptures. Because the earthquake occurred in the midst of a dense seismographic network, the fault plane

solution is extremely well determined (Whitcomb, 1971; Dillinger and Espinosa, 1971; Canitez and Toksöz, 1972). This mechanism is primarily thrust faulting on a northerly-dipping fault. Whitcomb et al. (1973) give the following fault plane parameters: strike, N67°(±6°)W; dip, 52°(±3°) to NE; rake, 72°(67°-95°).

Surface Faulting. With the exception of the dip, these parameters derived from the faulting in the hypocentral region agree well with those determined by examining the surface ruptures. This surface faulting has been described in detail by a number of authors and agencies, most notably Kamb et al. (1971), Palmer and Henyey (1971), and Proctor et al. (1972). The observed surface faulting can be broken into three main groups:

1. A fault line extending approximately westward from the mouth of Big Tujunga Canyon to Foothill Boulevard, labeled the Tujunga fault segment. Proctor et al. (1972) argue that the name Lakeview thrust fault is the appropriate appelation for this segment. Nevertheless, we will refer to this fault segment as the Tujunga segment so as to be consistent, no matter if incorrect, with previous work.
2. A complex group of short length semi-continuous faults located 0.3-0.9 km to the north of and

sub-parallel to the Tujunga fault segment. This group will be referred to later as the splay fault group.

3. A fault zone extending approximately westward from Pacoima wash to Sylmar. This fault zone is slightly over 1 km to the north of the Tujunga segment and is called the Sylmar segment.

The surface scarps of the Tujunga segment extend more or less continuously for 11 km at an average strike of N70°W. The observed dips on the well defined scarps are in the range 20-25° to the north, and the motion is shallow thrust and left lateral. In the sub-parallel splay group, the scarps tend to parallel the sediment bedding which dips at about 65° to the north. These faults have been identified as bedding plane reverse faults with about equal amounts of vertical and left lateral motion (Kamb et al., 1971). No direct measurement of the dip was possible on the Sylmar segment which extends about 3 km in an east-west direction. Unlike the Tujunga segment, the surface scarps are less well defined here, and the scarp displacements become more diffusely distributed (up to 50 m) toward the western end of this branch (U. S. Geological Survey Staff, 1971).

Aftershocks. The aftershocks of this earthquake have been studied intensely by a number of researchers. Hanks et al.

(1971), Wesson et al. (1971), and Allen et al. (1971, 1973) have described the location and depths of these events, and Whitcomb (1971, 1973) has gone into considerable detail interpreting the mechanisms and classifying these events. The epicentral locations of the aftershocks outline an area that is roughly crescent-shaped. The locations are clustered on the exterior of this outline indicating that, except at the edges perhaps, the stress was completely relieved in the region where the fault plane approached the free surface. The distribution also suggests that if we take the edge of the faulting plane to be defined by the outer limits of the aftershock distribution, then this edge is well defined. The hypocenter of the main shock is located at the lower, northernmost edge of this zone of aftershocks. Hanks (1972), Whitcomb (1971), Allen et al. (1973), and Whitcomb (1973) suggest that the western edge of the aftershock zone represents a steep flexure in the fault plane. The aftershocks along this flexure are predominantly left lateral strike slip and tend to occur at deeper depths than on the main fault plane.

Allen et al. (1973) give evidence for the fault plane to have an intermediate dip which is less than that obtained from the focal mechanism of the initial event but greater than the shallow surficial dips. These authors report that the slip motion vectors for the aftershocks

located between the hypocenter of the main event and the surface ruptures had an average plunge of 36° toward N 20° E. Additional supportive evidence for this intermediate dip angle for the fault plane between the two extremities is given by the calculated hypocentral depths of the aftershocks. Whitcomb et al. (1973) report that these events line up in a zone which has a dip to the north of between 35° to 40°.

4.3 Assumed Fault Model.

We have assumed the following fault system to conform with all the geological and geophysical properties that have been determined about this system which was discussed previously. The fault system is shown schematically in Figure 4.1. The main thrust branch of this system is composed of 21 adjacent fault elements. From the surface down to a depth of 7 km, these elements define a plane which dips at a constant angle of 35°. From 7 km to 9 km depth, the main thrust branch has a dip of 40°, and below this depth, each of the elements has a dip of 52°. The lower edge of the fault system is at a depth of 14.5 km. The splay fault system is modeled by a series of imbricate reverse thrust fault planes intersecting the main fault plane in the upper 1 km block. These 20 fault elements have a constant dip of 65°. We will see later in this chapter what effect the addition of these splay faults has

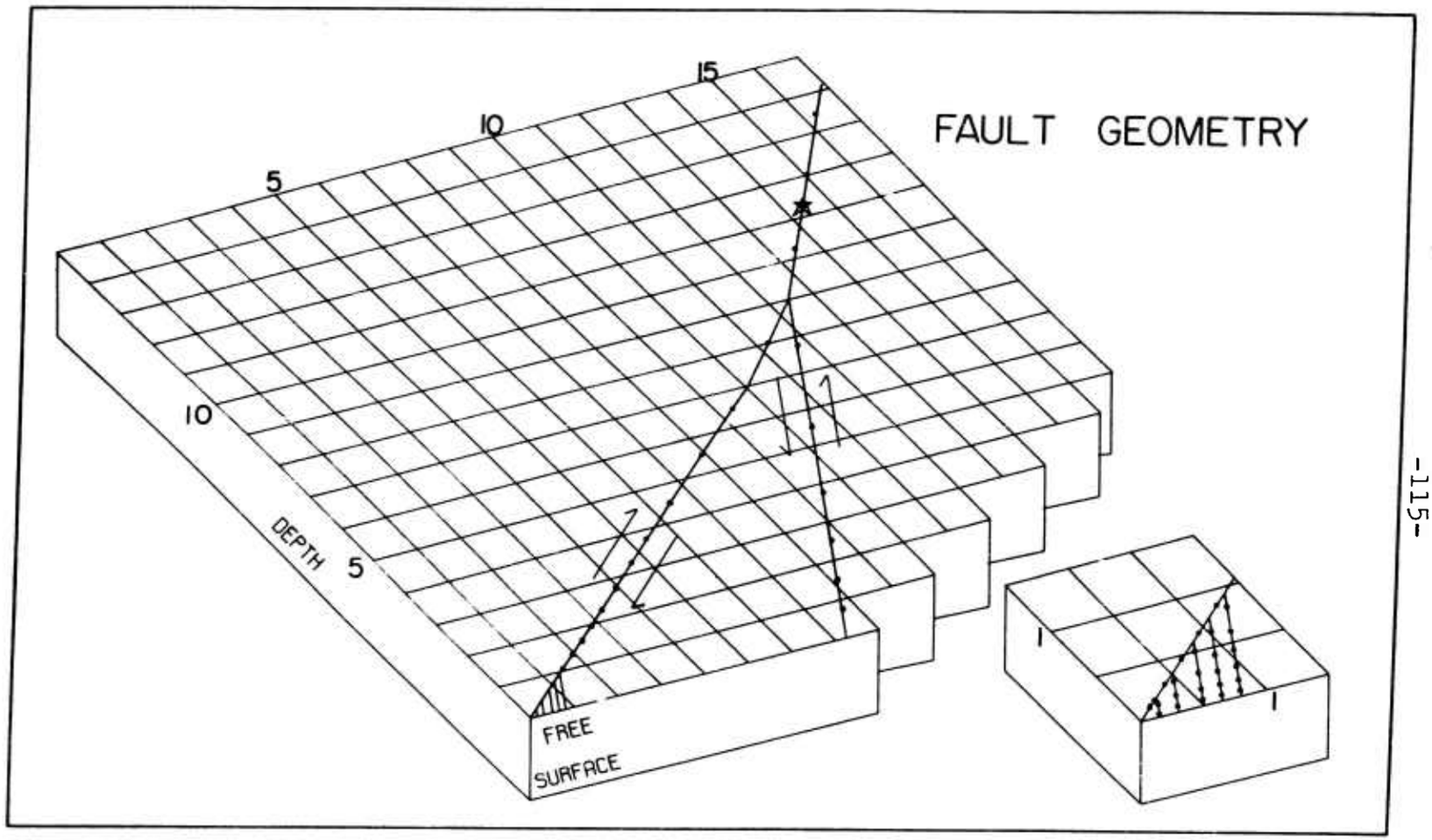

Figure 4.1. Perspective view of the assumed fault geometry. The solid circles indicate the mid-point depth (km) of the individual fault elements; the hypocenter of the event is indicated by the star. The block offset on the right is an expanded view of the upper 1.5 km to show the details of the splay fault group. The inversion profile extends from left to right along the surface.

on the calculated dislocation function. Also included in the fault system is a model of the San Gabriel fault. This fault is perhaps the major geologic feature of the entire epicentral area. Wesson and Wilson (1972) have postulated that this fault was involved in the seismic activity that accompanied this earthquake. Kamb et al. (1971) report, however, that there was no field evidence of displacement occurring on this fault in the aftershock region. We do note that there is a correlation of the area of positive gravity changes and the position of this fault. This suggests that if any displacement did occur on this fault during the earthquake, it occurred at depth, and the motion was of the normal faulting type. This fault is located some 7.2 km north of the main surface breaks on the Tujunga segment and is modeled by a plane of constant, 62°, dip composed of 6 fault elements. In this representation, the San Gabriel fault intersects the main thrust fault at a depth of 9 km. Thus, the total fault system is composed of 47 separate fault surface elements. Individual elements can be eliminated from the system by merely setting the weighting coefficient for that particular element to zero.

We have chosen to take the length of the fault elements near the surface to be 15 km. We have interpreted the clustering of the aftershocks in the epicentral area which form the top of the inverted "U" to be caused by the

fault length becoming somewhat less as the fault goes to greater depths. The fault lengths in our assumed model taper from 15 km at the surface to 9 km at the hypocenter. Table 4.1 gives the source parameters necessary for a description of this fault system. This table has been split into two parts. Part a gives the parameters for the fault elements which comprise the main fault. Part b gives the parameters for the splay fault group and the San Gabriel fault approximation.

In the fault representation given here, we have not accounted for the 1 km north-south offset between the Tujunga and Sylmar fault segments, but rather have considered the Tujunga segment as a continuous fault extending linearly over the surface for 15 km. Because this offset occurs close to a lateral extremity of the fault plane and we intend to choose our data for the inversion process from near the center of the fault plane, this approximation should be a good one. We will see later in this chapter how this offset can be modeled with the fault system geometry given here.

4.4 Static Data.

Although unfortunate from a humanitarian standpoint, the earthquake propitiously produced its maximum surface deformation in an area of exceptionally good geodetic control. This deformation was mainly mapped by measuring

TABLE 4.1a

Element #	Length	Dip	Mid Pt Depth	Width
M1	15	25°	0.050	.24
M2	15	25°	0.150	.24
M3	15	30°	0.275	.30
M4	15	30°	0.425	.30
M5	15	35°	0.600	.35
M6	15	35°	0.800	.35
M7	15	35°	1.050	.35
M8	15	35°	1.350	.52
M9	15	35°	1.650	.52
M10	15	35°	1.950	.52
M11	15	35°	2.300	.70
M12	15	35°	2.750	.87
M13	15	35°	3.250	.87
M14	15	35°	3.750	.87
M15	15	35°	4.500	1.74
M16	14	35°	5.500	1.74
M17	13	35°	6.500	1.74
M18	12	40°	8.000	3.11
M19	11	52°	10.100	2.79
M20	10	52°	11.950	1.90
M21	9	52°	13.450	1.90

Table 4.1a. Source Parameters for San Fernando Fault. Parameters are in km.

TABLE 4.1b

Element #	Length	Dip	Mid Pt. Depth	Width
S1	15	60°	0.25	0.12
S2	15	60°	0.075	0.12
S3	15	60°	0.04	0.12
S4	15	60°	0.11	0.12
S5	15	60°	0.18	0.18
S6	15	60°	0.04	0.12
S7	15	60°	0.13	0.12
S8	15	60°	0.22	0.23
S9	15	60°	0.31	0.22
S10	15	60°	0.04	0.12
S11	15	60°	0.13	0.12
S12	15	60°	0.23	0.17
S13	15	60°	0.31	0.17
S14	15	60°	0.44	0.31
S15	15	60°	0.04	0.12
S16	15	60°	0.13	0.12
S17	15	60°	0.24	0.17
S18	15	60°	0.34	0.17
S19	15	60°	0.46	0.23
S20	15	60°	0.60	0.28
SG1	15	62°	0.75	0.57
SG2	15	62°	1.50	1.13
SG3	15	62°	2.50	1.13
SG4	15	62°	3.75	1.70
SG5	14	62°	5.50	2.27
SG6	12	62°	7.75	2.83

Table 4.1b. Source Parameters for San Fernando Fault. Parameters are in km.

elevation and horizontal line length changes by comparing pre-earthquake and post-earthquake measurements. These data have been compiled principally by the U. S. Geological Survey (Burford et al., 1971; Savage et al., 1973), the City of Los Angeles, Bureau of Engineering (personal communication, 1971), and the Survey Division, Department of County Engineer, County of Los Angeles (1971). From these sources, over 100 vertical displacement data points were obtained. These points were then plotted and contoured for equal elevation changes. This contour plot is shown in Figure 4.2. With the exception of a few points located just to the south of the surface ruptures, all the data points obtained from the geodetic releveling show an uplift. In addition to the releveling data, we can estimate changes in elevation by examining the changes in the gravity field caused by this change in elevation. For this earthquake, we have measured gravity changes in unsurveyed areas where elevation changes would otherwise be unattainable. Appendix 2 of this thesis describes the gravity changes which accompanied this earthquake and the relationship between the measured elevation changes and the gravity changes.

Figure 4.2 also shows a profile which approximately bisects the area of deformation. In this study, we will limit our inversion data set to vertical displacement data

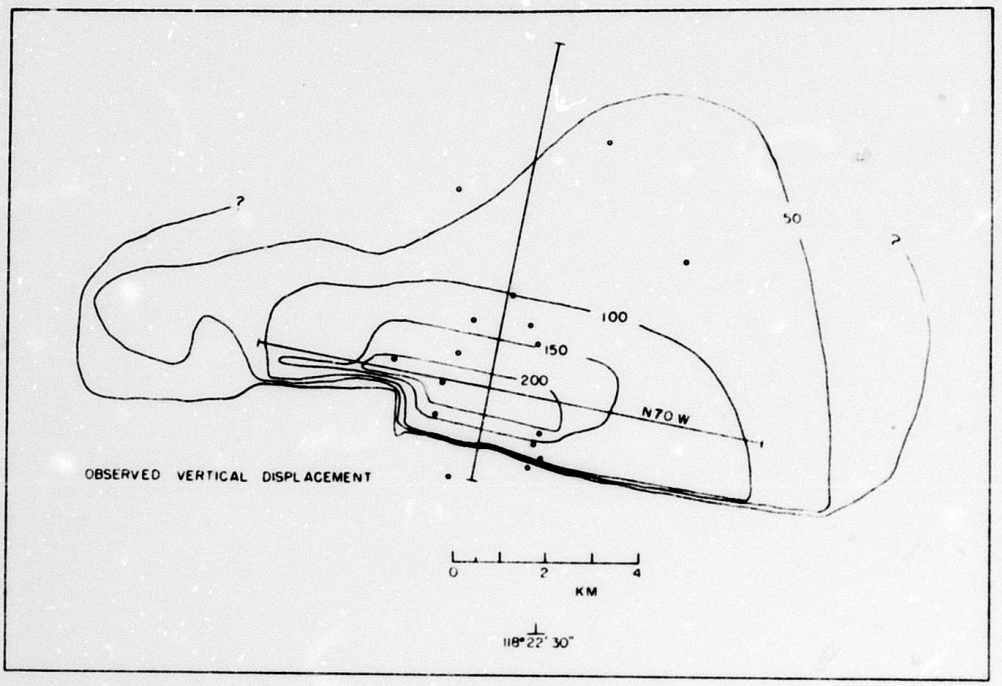

Figure 4.2. Contour plot of observed vertical static displacements. Open circles indicate the location of the data values used in the inversion profile. Profile is indicated as the line perpendicular to the strike of the surface deformation.

only. An attempt was made to use horizontal shortening in the direction perpendicular to the strike of the fault, but the only data which were least contaminated by end effects were relative line changes between stations both of which were located very near the surface ruptures. These data are shown in Figure 4.3 (eg. TUJ-6P10). This kind of data is particularly ill-suited for inclusion in the inversion because if the surface ruptures are mislocated by even 10-20m, the relative line change can change drastically. Since the Tujunga scarp has this much local variation in linearity, we considered these data too unstable to use in the inversion scheme. We therefore limited the inversion data set to vertical displacements only.

As in the case of the Alaska earthquake, we restricted our data set to only those points which could be projected onto a profile without crossing a contour line. There were 16 releveling points near the profile which met this criterion. These points are shown in Figure 4.2. It is seen on this figure that along the profile the contours for displacements greater than 100 cm are quite regular. By regular, we mean that they are orthogonal to the profile. On the 50 cm contour line north of the surface ruptures some asymmetry is apparent. Since we wanted to include information over as much of the profile as possible, we

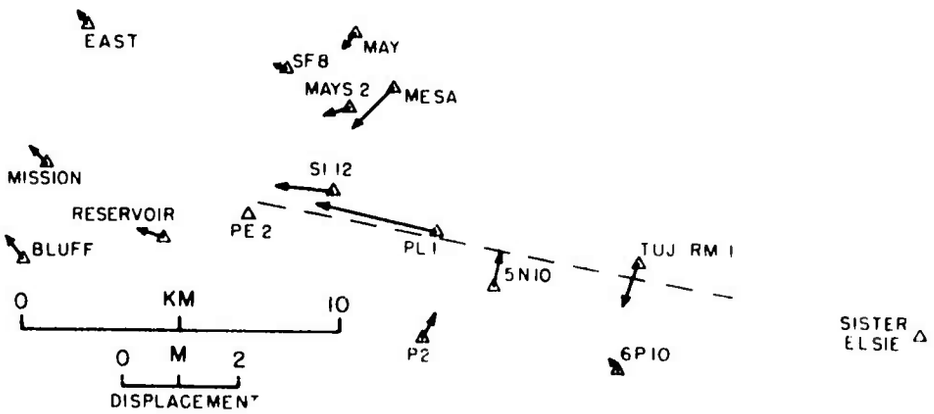

Figure 4.3. Horizontal displacements (relative length changes) in the area (Savage et al., 1972; reproduction permitted by Dr. J. C. Savage).

decided to include an estimation of the displacement here. The data point between the 50 cm contour line and the 0 cm contour line to the west of the profile shows 35 cm of uplift, and the data point within the 50 cm contour line to the east of the profile indicates 65 cm of uplift. The 50 cm contour line was drawn halfway between these two points, and a 50 cm data value was included into the inversion data set at the point where the 50 cm contour line intersected the profile. In making this approximation, we have included a larger variance to this point. We will see later that a lateral variation of $\pm$ 0.5 km of the location of this particular data point along the profile does not degrade the fit of our final model. There are other releveling points along this profile in the epicentral area along Sand Canyon Road. The vertical displacement values of these points range from 25 cm to 30 cm over a length of 2-3 km. We have chosen to include this cluster of points as a single value of 25 cm and to increase the variance associated with this datum. This was done because Ellingwood and Williamson (1971) report that these points might have as much as 8-11 cm of uplift due to secular change.

Four more vertical displacement data points were added to the inversion data set by converting gravity changes to elevation changes. Three of these points are located to

the north of the points shown in Figure 4.2, but still south of the epicenter. One point is located north of the Sand Canyon Road releveling points. The exact locations of these gravity points are shown in Figure A2.4 given in Appendix 2. Further discussion about the gravity points can be found in that section of this thesis.

In this investigation, we will assume that all the vertical displacement occurred at the time of the initial earthquake. Displacements occurring after this main event were found by a number of surveys to be very minor when compared with the total vertical displacement (Nason, 1971; Lahr et al., 1971; Burford et al., 1971; Savage et al., 1973; Sylvester and Pollard, 1973). Any vertical afterslip that was measured for a particular datum is included in the variance of the displacement for that datum.

Table 4.2 gives the entire data set that we will use in the inversion. The origin of the profile is taken at the surface breaks with positive distance taken to be in the direction of N 20° W. Also included in this table is the estimated error in the data. This error estimate is taken to be that estimated by the individual investigators who measured the data.

4.5 Calculated Dislocation Model.

Starting Model. Since several other investigators (Savage et al., 1973; Canitez and Toksöz, 1972) have proposed a

TABLE 4.2

Distance (km)	Δz (cm)	δ(Δz) (cm)	Reference Year	Source
-0.73	-1.0	3.0	1960	LABE
-0.23	-3.0	3.0	1960	LABE
0.22	114.0	4.0	1963	USGS
0.34	142.0	4.0	1963	USGS
0.50	185.0	4.0	1963	USGS
0.55	192.0	4.0	1963	USGS
1.26	228.0	4.0	1963	USGS
1.48	207.0	4.0	1960	LABE
1.87	173.0	4.0	1963	USGS
2.40	149.0	4.0	1963	USGS
2.66	122.0	6.0	1963	USGS
2.78	135.0	6.0	1963	USGS
3.42	98.0	4.0	1963	USGS
4.82	71.0	4.0	1929	USGS
6.52	50.0	8.0	*	USGS
8.22	29.0	13.0	**	USGS-GRAV
9.92	0.0	13.0	1970	GRAV
11.50	-15.0	20.0	1970	GRAV
17.00	22.0	17.0	1964	GRAV-USGS
20.00	10.0	17.0	1964	GRAV

* Average - 65 cm (1929) and 38 cm (1960)
** Average along Sand Canyon Road (1963-1968)

Table 4.2. Vertical uplift data along Inversion Profile. Distance is measured from origin of profile, Δz is the uplift, δ(Δz) is the estimated uncertainty of the measurement. LABE = Los Angeles Bureau of Engineering, USGS = U. S. Geological Survey, and GRAV = Gravity measurements (see Appendix 2).

constant dislocation on some constant-dipping fault plane to be consistent with the static data for this earthquake, one such starting model would be to assume a constant dislocation throughout the assumed main fault system. A simple numerical experiment was devised to test the applicability of this constant dislocation model to the inversion data set. This experiment is described as the following.

From Table 4.2 we see that the maximum vertical displacements occur at about 1 km to the north of the origin of our fault system. (The origin of the fault system is taken as the point where the Profile AA' intersects the line formed when the main fault surface intersects the free surface.) If we normalize the observed displacement data to this maximum value, we see that there is a rapid diminution with distance away from the surface ruptures. One way of affecting this rapid distance-decay of the vertical displacements is to have the fault plane dip at a steep angle. In the case of this earthquake, the dip of a single fault plane representation is limited by the spatial relationship of the surface ruptures and the epicentral location. If we assume that the hypocenter marked the lower bound of the fault plane, then the maximum angle that a single plane could take would be about 45°. This takes into consideration the uncertainty in the

locations of both the epicenter and hypocenter. Another factor that affects the vertical displacement at distance away from the surface ruptures is the depth to the bottom of the fault plane. In this problem, this is correlated with the fault dip. The minimum value of depth that this fault plane could take would be about 9 km. If we calculated the vertical displacement from a fault plane with these parameters, we see that the diminution is much smaller than that exhibited by the data. These results after a similar normalization are shown in Figure 4.4. For a more reasonable geometry of a constant dip of 35° and a depth of faulting of 10 km, the fit to the data is even worse. Intermediate to these two curves in this figure is that for a fault plane dipping at 45° and extending to a depth of 12 km.

One might argue that local geologic heterogenities might cause such a departure from the idealized elastic case for which we have assumed in these calculations. This same experiment can be carried out with the finite element modeling technique. When the geologic structures of this area are used in this technique, practically the same results are obtained (Jungels, personal communication, 1972).

If we take a planar dislocation surface of constant dip, but allow the displacement to vary along this surface, we can fit the observed vertical displacement much better

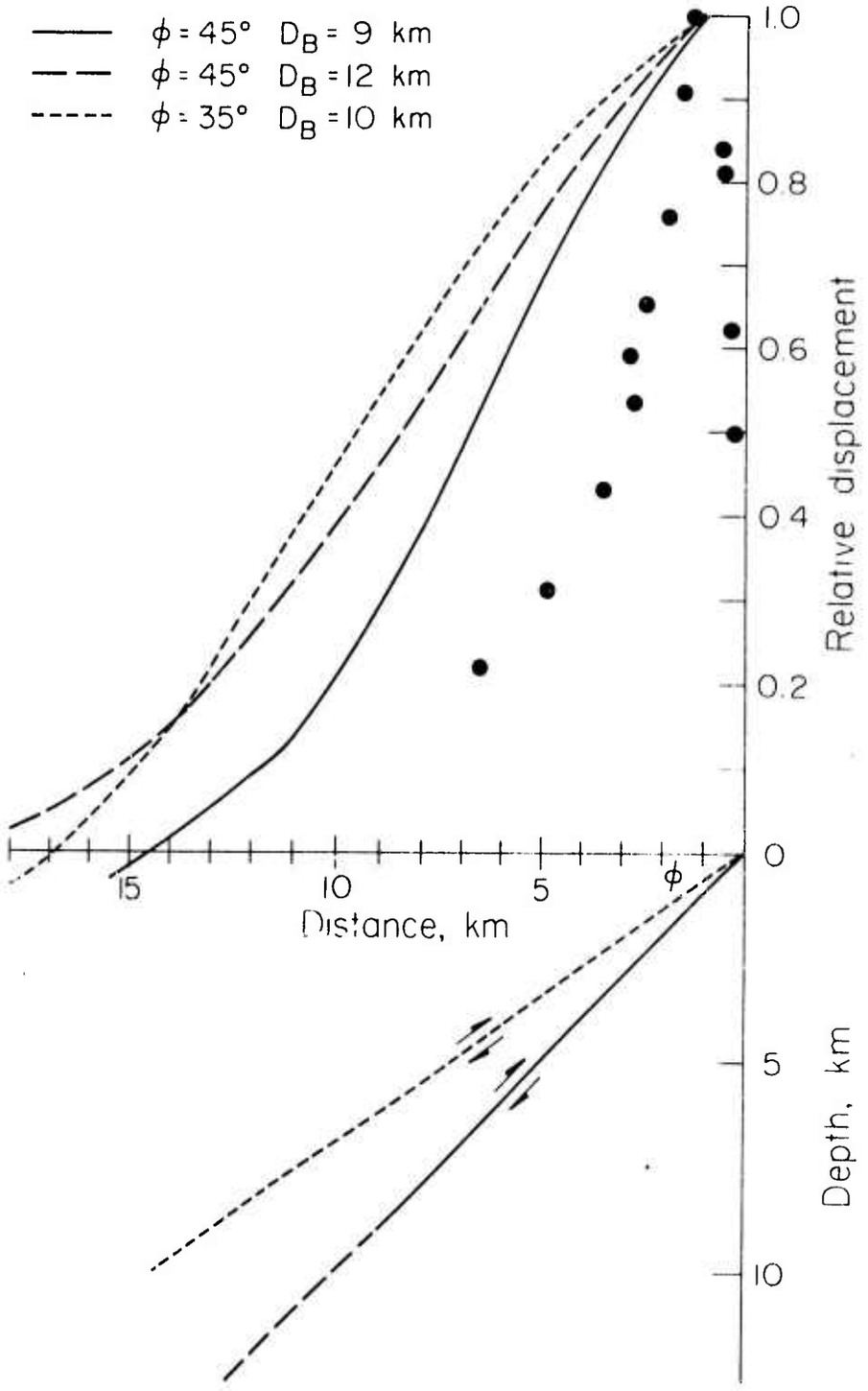

Figure 4.4. Test to see if a constant dislocation on a fault surface could fit the observed vertical displacements. The data (solid circles) are normalized to the maximum value.

if the displacement is allowed to vary piece-wise with depth in a manner $e^{-\gamma h^2}$. No inversion was used in these calculations, but rather different slip models, each having a different slip decay-rate away from the surface, were tried. The constant, γ, necessary to fit the data in this case can vary from 0.07 km^{-2} to 0.12 km^{-2} depending on the chosen dip of the fault plane. Mikumo (1973) has arrived at a similar result.

This simple calculation has been rather unsophisticated, but we think that this illustration clearly shows that the observed vertical displacement data require a fault dislocation function which varies along the fault. This variation in the fault slip should be in the direction of decreasing with increasing depth in order to properly fit the data. Since we have normalized the amplitudes to that obtained about 1 km distance from the point at which the fault surface intersects the free surface, this conclusion might not hold for the upper 1 km (approximately) of the fault surface.

We can now proceed with the actual inversion of the displacement data to get the "best fit" dislocation function. We will use as a starting model one in which the displacement varies in an exponential manner as that described above. We can note here that we would intultively expect that the displacement data shown in Figure 4.4

would be affected by only the upper 5-7 km of the fault system that we have chosen. This fault system was made to consist of many small fault elements in order to more adequately estimate this large slip variation which we will expect.

Inversion Results. The media response matrix, **A**, was calculated from the analytic expressions given by Mansinha and Smylie (1971) for the structural model given in Table 4.1. Using this formalism, the static displacement response on the surface at the positions of the observed data due to a unit (1 cm) dislocation on each of the individual fault elements was calculated. Since there were 20 data points, or 20 positions on the surface at which the displacement response was calculated, the media response matrix was composed of 20 rows. The number of columns of the matrix indicates the number of fault elements which were used to represent the fault system. This number was varied, as we shall see below.

Initially, we assumed that the fault system was composed of only the 21 elements listed in Table 4.1a (M1-M21). We will refer to this fault system as the main thrust sheet. The media response matrix for this fault system was composed and the inversion scheme initiated with the exponental decay starting model described in the previous section. The inversion converged quickly to a

"best fit" solution. This solution is presented in Figure 4.5.

The lower part of Figure 4.5 shows this "best fit" dislocation on each of the 21 fault elements which comprise this present fault system. We see that the dislocation at the surface is calculated to be 266 cm. This value immediately decreases to 160 cm at a depth of about 0.3 km. The maximum dislocation (515 cm) on the fault surface is at a depth of 0.8-0.9 km. At depths greater than 1 km, the dislocation on the fault surface decays almost linearly. A minimum is reached at about 8.5 km depth, and the dislocation function increases slightly in the hypocentral region. The maximum displacement in the hypocentral region in this case is 140 cm. The resolvability of the features of this particular model will be discussed in a later section.

The displacement at the surface due to this particular dislocation function was calculated along a profile at 0.2 km increments. This displacement profile is shown in the upper part of Figure 4.5. The observed displacement data as projected onto this profile are indicated along with the estimate of their errors. In this figure, we see that for the observed data located to the north of the surface breaks (given by positive distances along the abcissa in the figure), the fit as given by this "best fit" model is

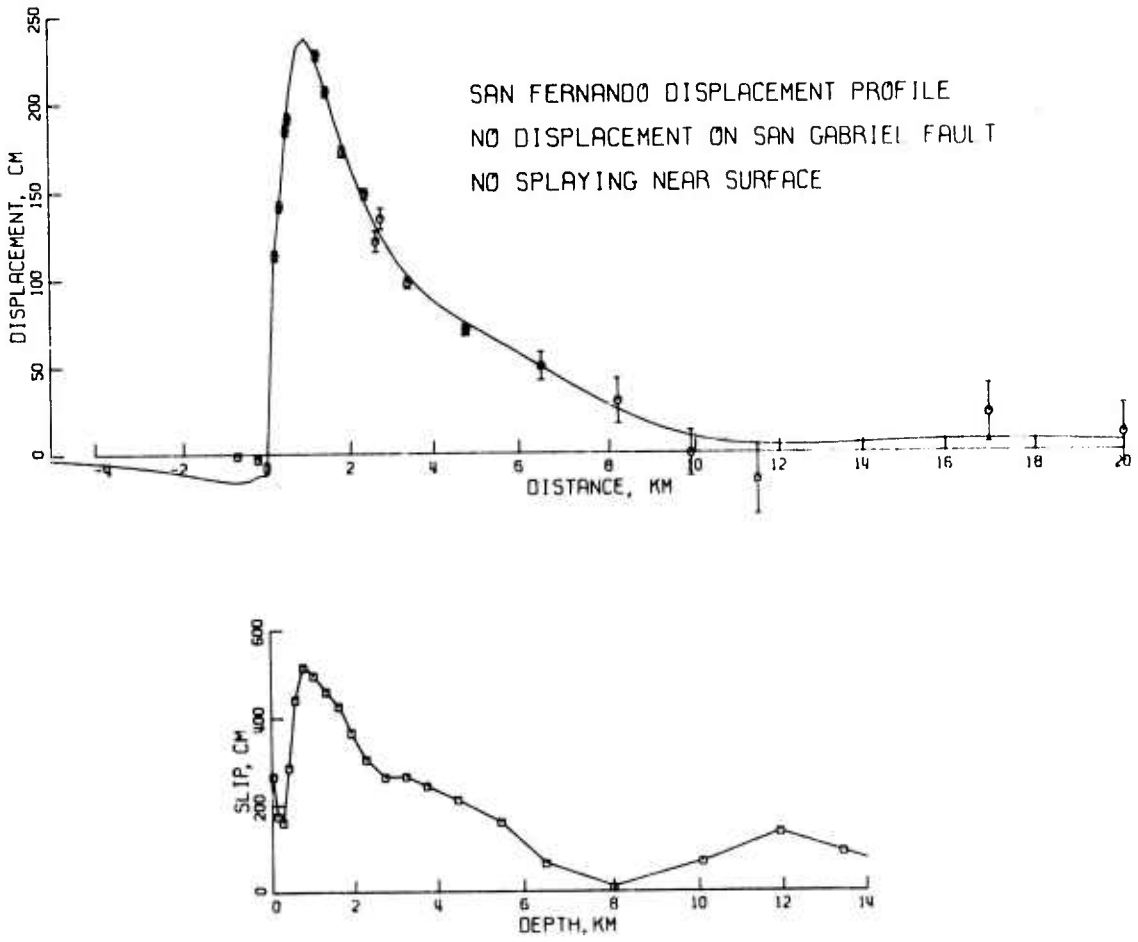

Figure 4.5. Lower--Best fit dislocation function for the main thrust sheet. Upper--Comparison of the calculated surface displacements from this model to the observed profile data.

quite good. To the south of the surface breaks, the calculated model predicts too large a negative surface displacement than is observed. A noteworthy feature of this particular fit is the importance, as far as spatial coverage along the profile is concerned, of having included the gravity-converted displacement points in the inversion data set. These converted data points force the calculated displacement field to go through a slight minimum in the profile distance 10-13 km away from the surface breaks. The displacements at distances greater than at the point where this minimum occurs are dependent almost totally on the dislocation function in the hypocentral region. The RMS error residual (observed-calculated) for all the data is about 8 cm.

In the next figure (Figure 4.6), we see what effect there is on this "best fit" solution when we exclude from the inversion data set the gravity-converted displacement data. In this figure, we see that the dislocation function along the upper 6 km of the fault system is essentially unchanged. Below this depth, the dislocation minimum along the fault sheet is reduced from what was previously calculated and shifted to a slightly smaller depth. Larger dislocations (maximum-275 cm) are now given in the hypocentral region. However, we note that only one data point, located at 17 km along the profile, is controlling the

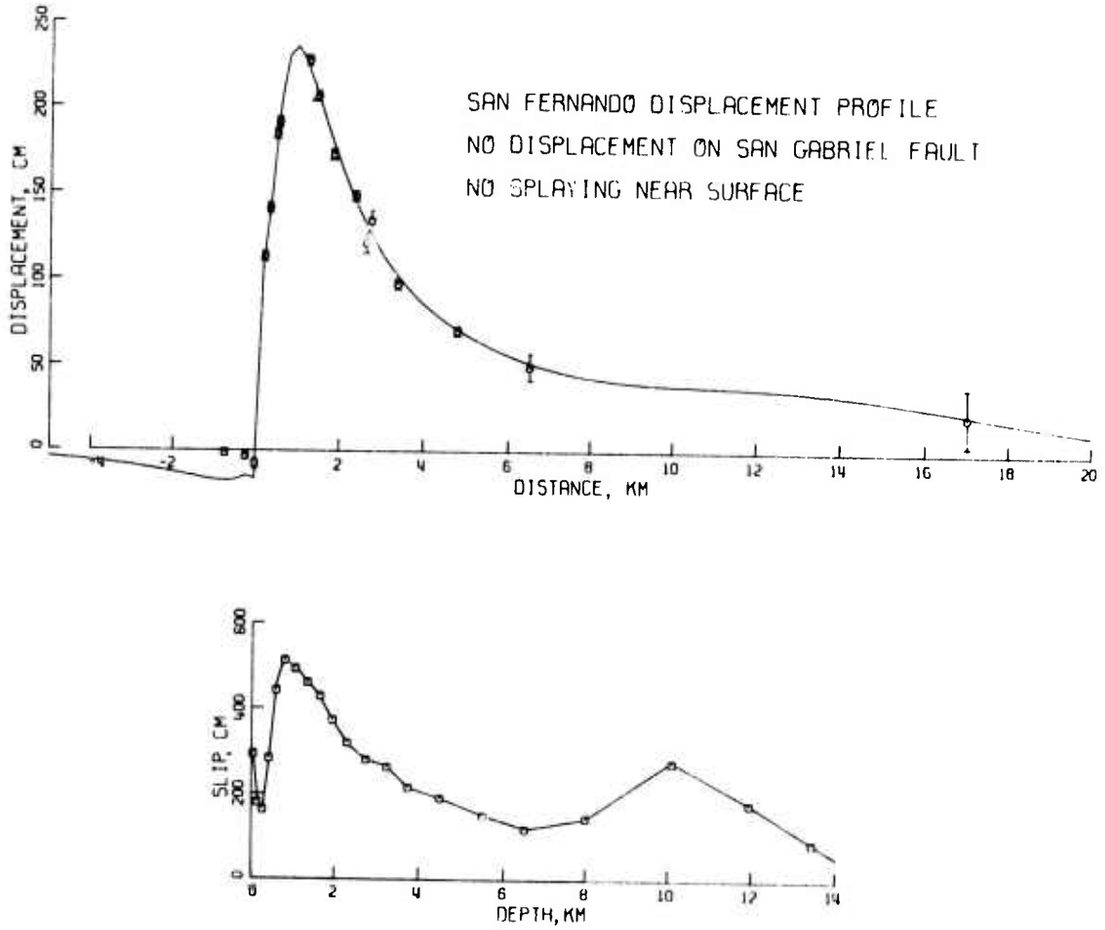

Figure 4.6. Lower--Best fit dislocation function for main thrust sheet when gravity-converted data points are excluded from inversion data set. Upper--Comparison of the calculated surface displacements from this model to the observed profile data.

amount of dislocation in this region. The resolvability of the dislocations in the hypocentral area will thus be highly dependent on the variance of this one data point. In the section on averaging in this chapter, we will see how the inclusion of the gravity-converted displacement data, inaccurate as they are, affects the resolution in the hypocentral area.

Next, we want to look at the effect of including a representation of the San Gabriel fault into our fault system for which we will use the inversion scheme to obtain a dislocation model. The structural parameters for this addition, which is composed of 6 elements, are given in Table 4.1b (SG1-SG6). The media response from these elements was computed and included in the response matrix. Figure 4.7 shows the results of the inversion of the data set (including the gravity-converted points) for this particular fault system. Comparing the dislocation function found in this figure and that obtained by the single thrust sheet (Figure 4.5), we see that practically the only difference between the two models is the amount of fault dislocation in the hypocentral area. In this present model, the slip in the hypocentral area is about 60% greater than that shown in Figure 4.5. This larger displacement in this region is necessary to accommodate the slip calculated for the San Gabriel fault. The slip

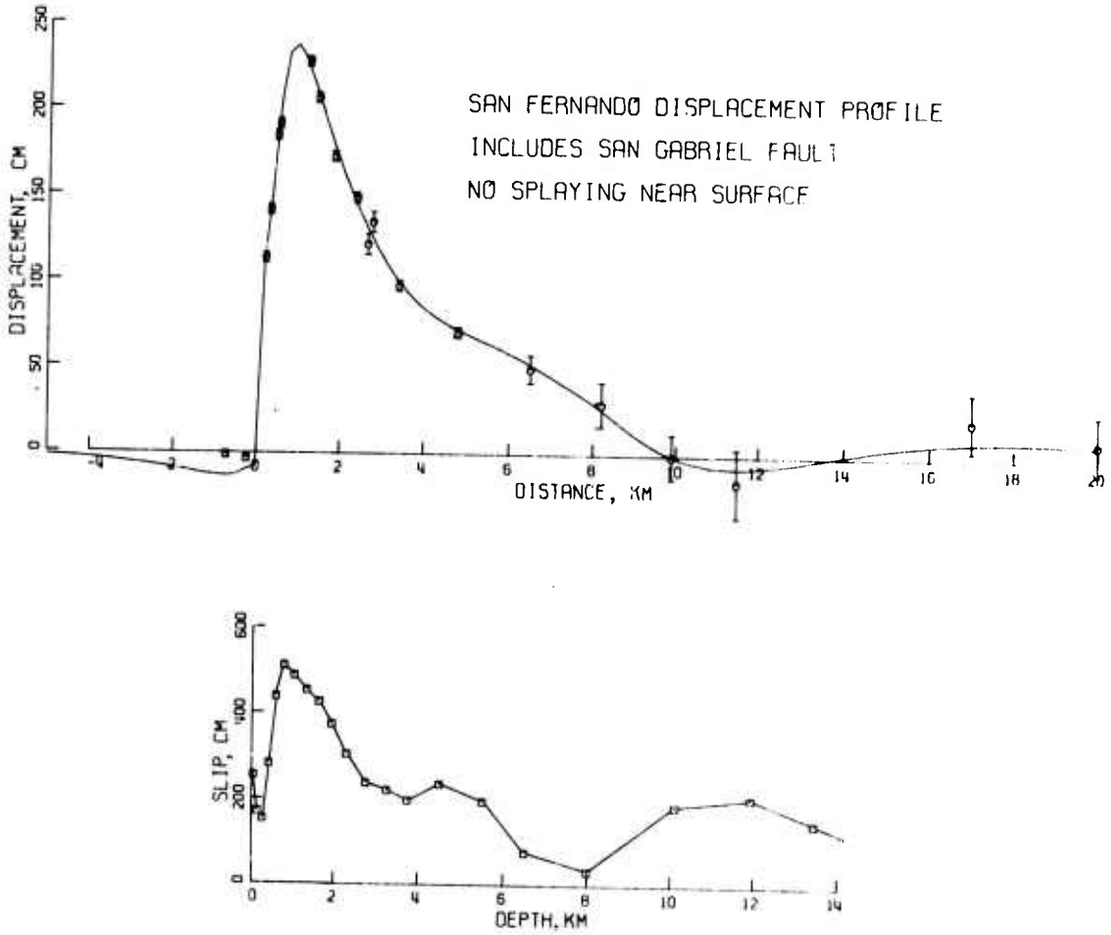

Figure 4.7. Lower--Best fit dislocation function for the main thrust sheet and San Gabriel fault representation. Upper--Comparison of the calculated surface displacements from this model to the observed profile data.

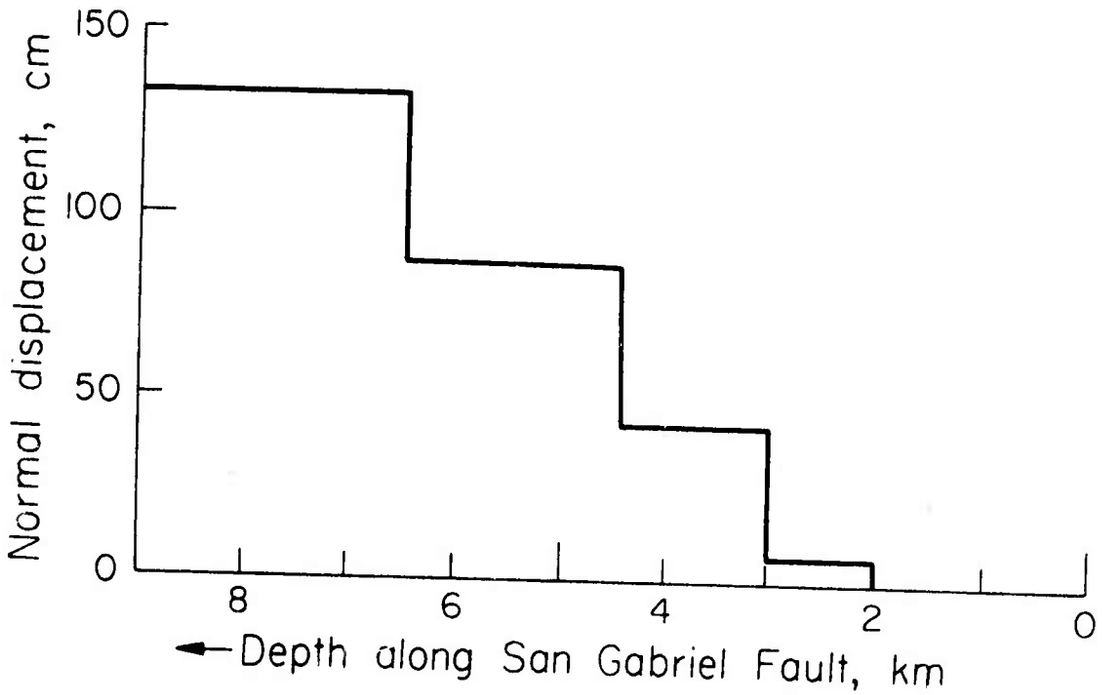

Figure 4.8. Best fit solution for normal slip on the San Gabriel fault representation.

calculated for the elements representing the San Gabriel fault is not shown in Figure 4.7 but is indicated in Figure 4.8. The sense of motion of the slip calculated on the San Gabriel section is opposite that on the main thrust sheet, i.e. normal faulting. We see here that the normal slip decays rapidly almost linearly toward the surface. This model predicts no motion on this fault for the upper 2 km, agreeing with the lack of observable expressions of surface motion on this fault after the earthquake (Kamb et al., 1971). A later section of this chapter goes into detail about whether this slip is required by the data.

Some mild supportive evidence for the existence of normal faulting on the San Gabriel fault representation is given in the following discussion. Whitcomb et al. (1973) give a strong correlation to the noted areas of compressional release (normal faulting) as determined by focal mechanism studies and the area of mapped gravity increases. If the areas of the San Gabriel fault representation that were computed to have undergone normal faulting were projected to the surface, then this projection would approximately coincide with the area of gravity increase and the correlated compressional release.

Calculation of the averaging operator (equation (2.29)) for this structural model reveals a strong coupling between thrust slip in the hypocentral area and normal slip along

the lower part of the San Gabriel fault representation. This coupling is in the sense that in order to keep the same displacement at the surface while increasing the thrust displacement in the hypocentral region, it would be necessary to increase the normal slip along the lower part of this auxiliary fault. This coupling is illustrated by the results shown in Figure 4.9. In this figure, we have significantly increased the dislocation in the hypocentral area. Hanks (1974), on the basis of an analysis of the Pacoima Dam strong motion records, postulated that this earthquake initiated with large (4-9 m) ruptures in the hypocentral region. In this example, we will see if the surface static displacement data support this hypothesis. In this calculation, we have initially set the fault dislocation for the three bottom fault elements of the main thrust sheet at the levels indicated in Figure 4.9. In the inversion calculations, the model weights for these elements were set such that these three dislocation values remained fixed. The result from the inversion is the smooth model given in the figure. The fit to the observed data for this particular model is extremely good, with the RMS error residual found to be less than 5 cm. We see that the minimum in the fault dislocation function is shifted to a much shallower depth than in previous examples. The dislocation function calculated for the upper part of the

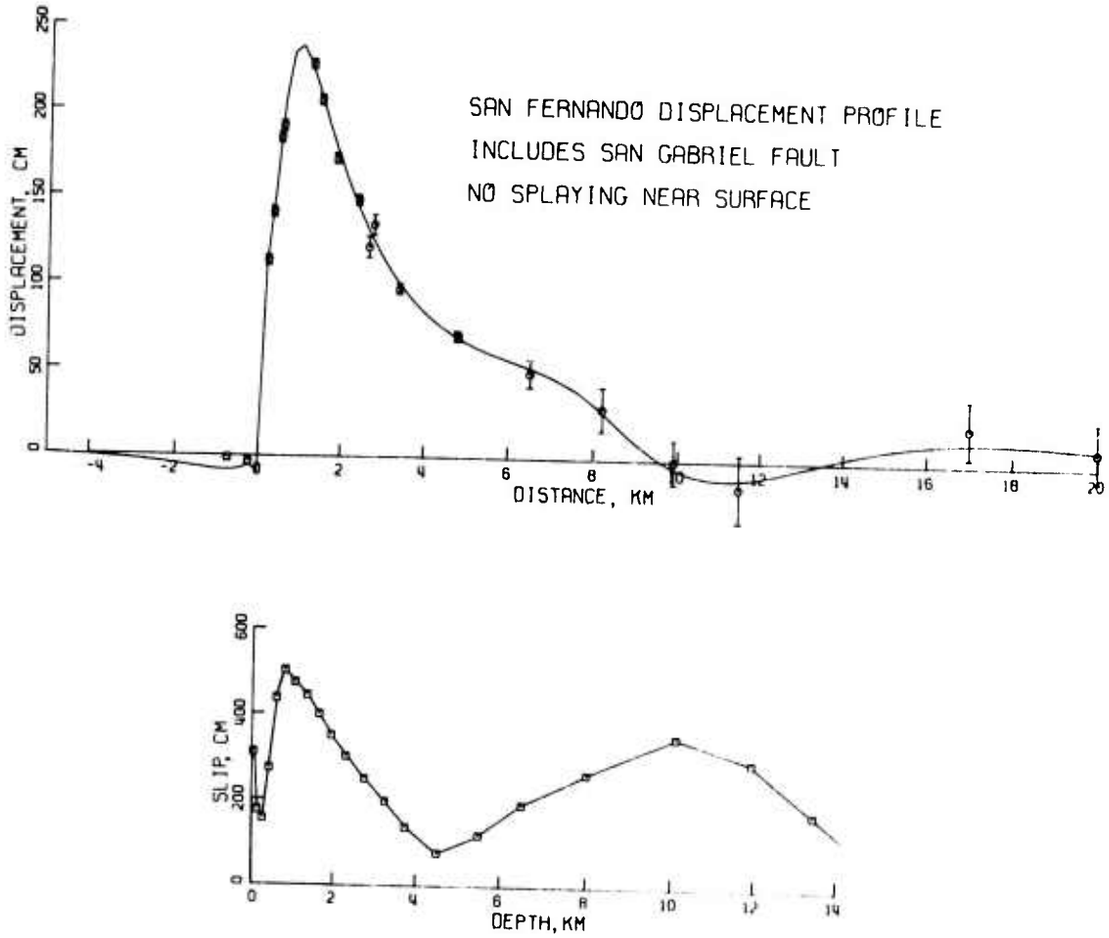

Figure 4.9. Lower--Best fit dislocation function for the main thrust sheet and San Gabriel fault representation when large displacements are forced in the hypocentral region. Upper--Comparison of the calculated surface displacements from this model to the observed profile data.

fault sheet is the same as before. However, the maximum normal slip on the San Gabriel fault has been increased to almost 300 cm -- approximately double that shown in Figure 4.8. The dislocation function on the auxiliary fault retained the relative shape as that shown in Figure 4.8.

We next include the splay group of fault elements into our fault system. The structural characteristics of these elements are listed in Table 1b (S1-S20). The media response to these elements was calculated, and the response matrix was expanded to include these values. For comparison, we chose as our starting model for the inversion the final model given in Figure 4.9. The results of this inversion are shown in Figure 4.10.

A comparison of the slip model in this figure and that shown in the previous figure reveals that the two models are practically identical except for the upper 1.5-2.0 km. This is to be expected since the fault geometry was only changed for the upper 1 km, and we would expect this small part of the fault system to be relatively uncoupled from the rest of the fault system. For this model, the fit to the data to the north of the surface ruptures is equally satisfactory as with the unsplayed fault geometry, but the fit to the two data points to the south of the surface ruptures is degraded somewhat. For the dislocation on the main thrust sheet near the surface, instead of varying

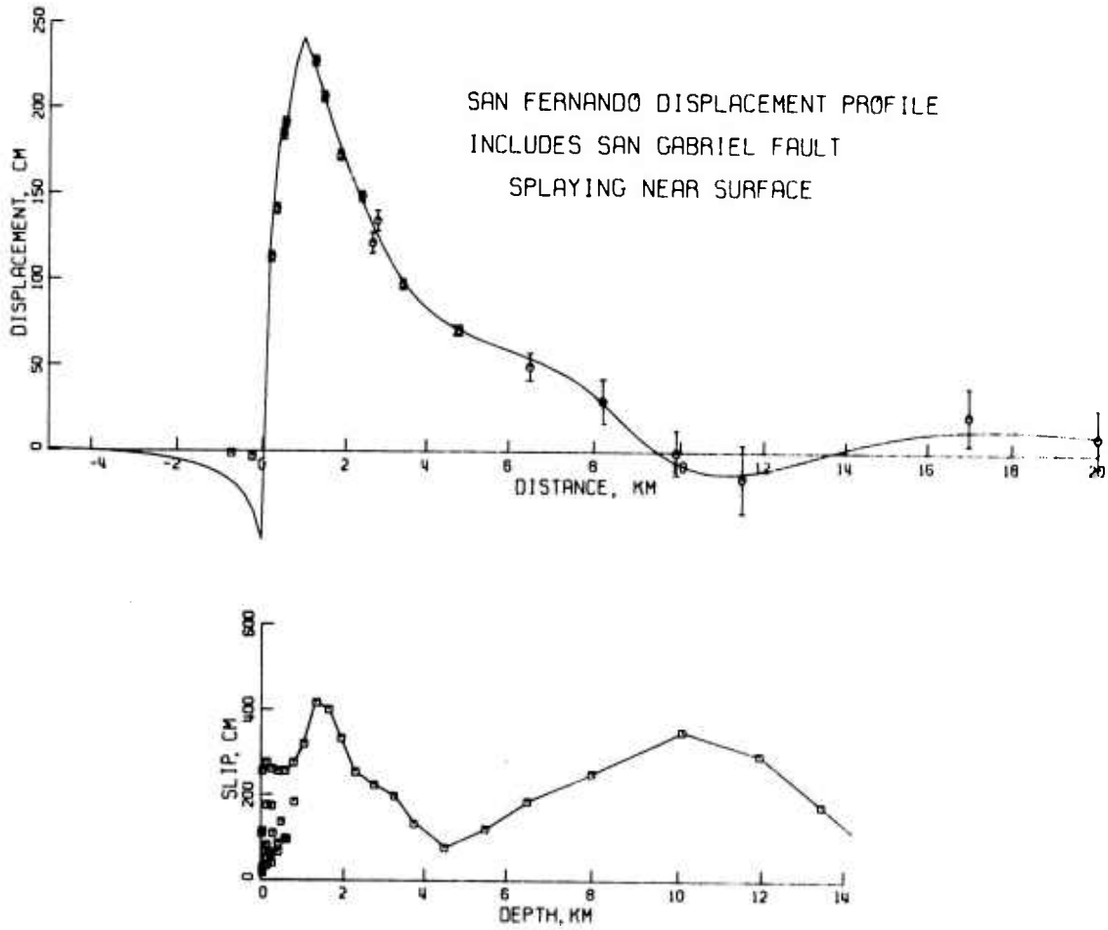

Figure 4.10. Lower--Best fit dislocation function for fault system when near-surface splay faults are introduced. Upper--Comparison of the calculated surface displacements from this model to the observed profile data.

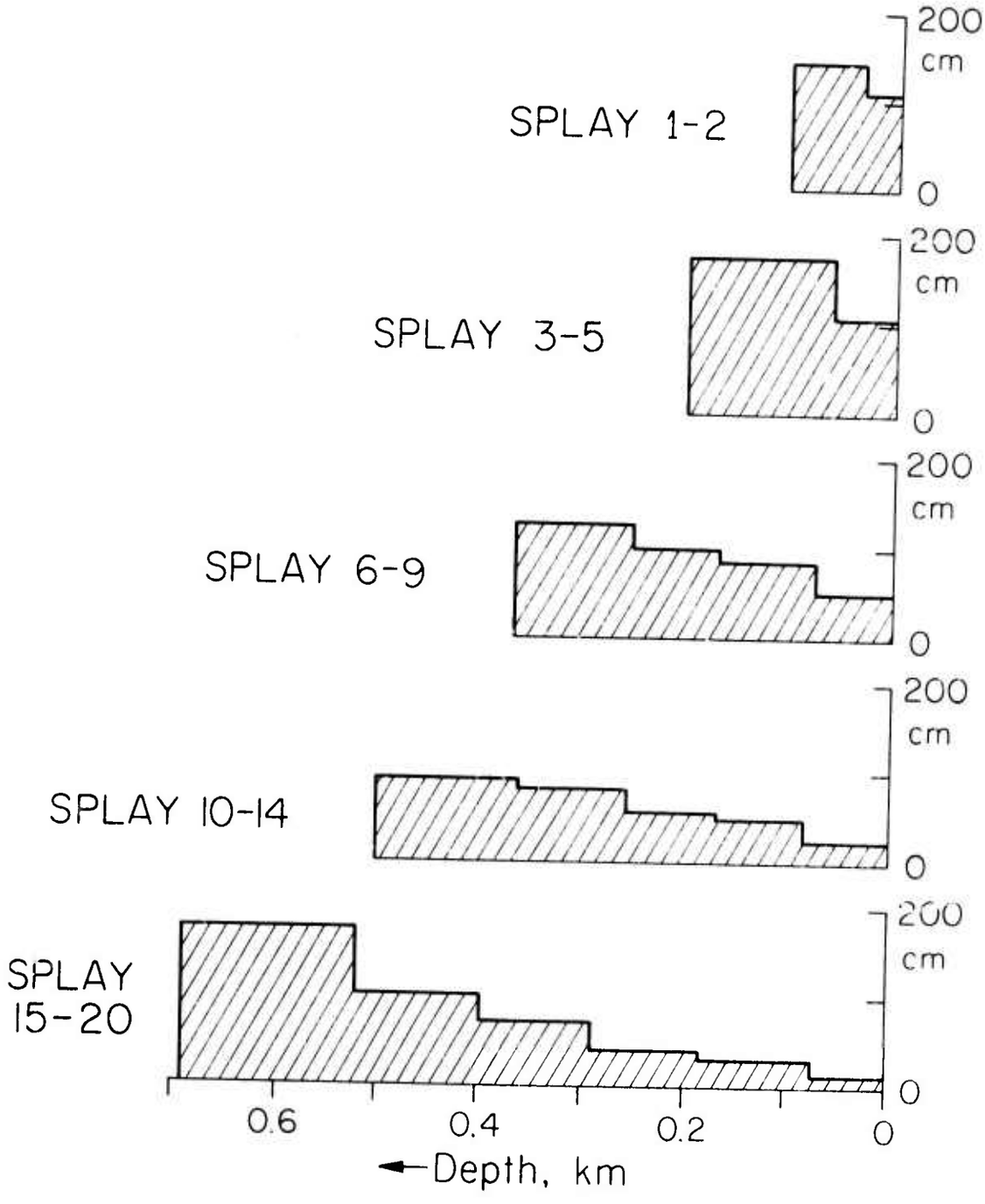

Figure 4.11. Best fit solution for slip on the near-surface splay faults.

rapidly as in Figure 4.9, the slip is almost constant at 250 cm, and the maximum slip on the thrust sheet is reduced by about 20% to 400 cm. The slips on the small splay faults vary smoothly away from the value on the main thrust sheet where they intersect that sheet. The slip on the splay faults is better illustrated in Figure 4.11. Here we see that not only does the calculated slip decay smoothly toward the surface, the displacements at the surface decrease away from the surface ruptures.

Since we have limited our inversion data set to points which were located near the profile which approximately bisects the observed surface deformation, we would now like to see how the calculated displacement from this model compares to what is observed in areas away from this profile. For observation points away from the center of deformation, one must consider the contribution to the vertical displacement caused by any strike slip component of fault dislocation. In this calculation, we will arbitrarily assume that the dislocation slip vector on each of the fault elements has a constant rake angle of 60°. This is about the maximum component of left lateral motion that would be allowable based on the focal mechanism data of Whitcomb et al. (1973). At this rake angle, the left lateral strike slip dislocation is 0.6 of the pure dip slip component. For the majority of the observations, the

calculated vertical displacement from the strike slip component of dislocation is a secondary effect.

One obvious feature of the observed surface vertical displacements is the offset between the Tujunga and Sylmar fault segments. This offset is easily modeled by slightly altering the geometry of the upper part of the fault system. An advantage of including the small splay faults near the surface, in addition to approximating the surface ruptures observed north of the main Tujunga scarp, is that it allows one to easily model the observed offset in the surface faulting. This is done by letting the upper six elements of the main thrust sheet and all the splay fault elements (S1-S14), except the ones fartherest from the main surface breaks, terminate at the Tujunga-Sylmar offset. This means that these particular fault elements have lengths of only 10 km with the coordinate system origin of these elements shifted 2.5 km to the east. The total contribution to the surface deformation from all the fault elements was calculated taking into consideration this lateral offset where appropriate. The results are shown in Figure 4.12. The fault dislocation function used for these calculations is the same as that given in Figure 4.5 with the addition of the splay fault system.

A comparison of the contours presented in this figure and the areal displacement given in Figures 4.2 and A2.4

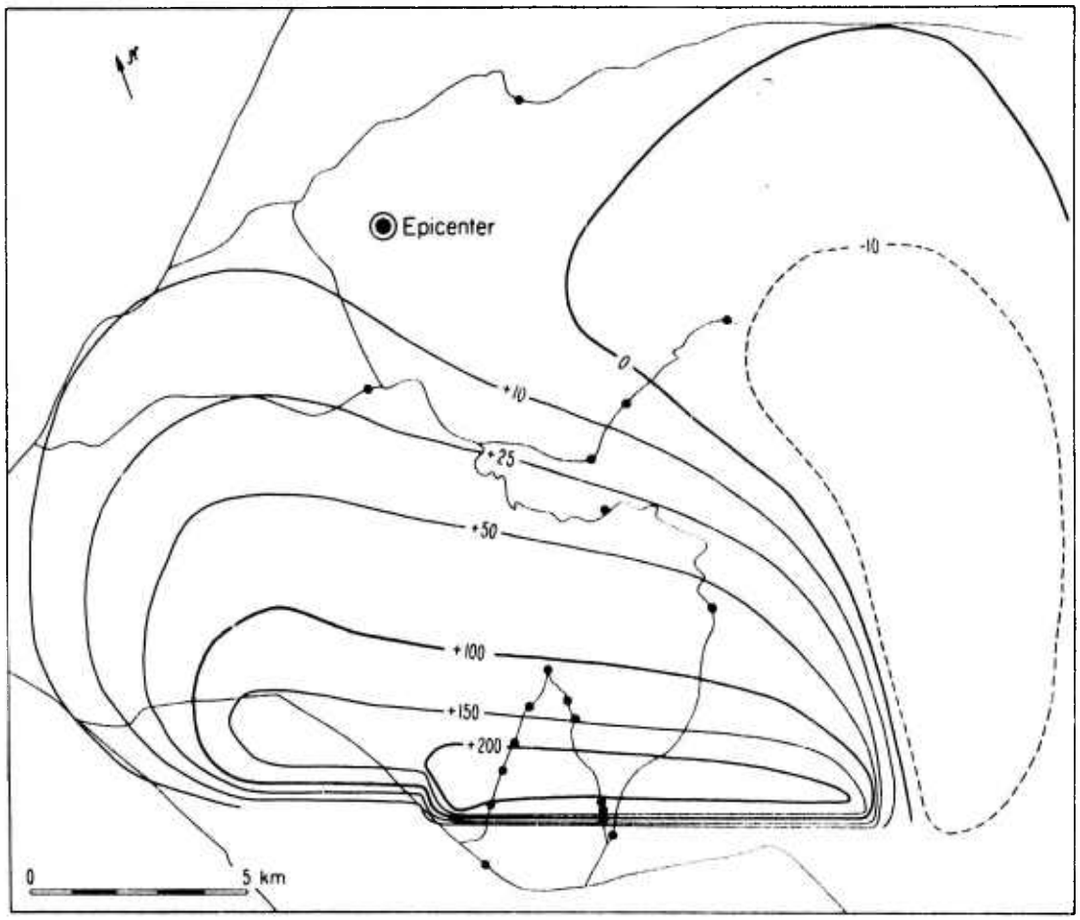

Figure 4.12. Computed vertical displacement field from best fit model given in Figure 4.5 with the addition of the near-surface splay faults. The fault dislocation includes a component of left-lateral strike slip taken to be 0.6 that of the dip slip motion. Contours are in cm of uplift. The solid circles show the location of the data used in the inversion. Superposed on the contours is a map of the roads in the area.

shows the degree of fit the calculated model has to the observations. If instead we had used the dislocation function like that indicated in Figure 4.7, the effect on the area deformation would be to increase the magnitude of the downward displacement in the northeast area and to increase the northward extent of the 10 cm contour line. For contour levels 25 cm and above, there is practically no discernible difference between the two plots.

One feature of Figure A2.4 which does not appear in the theoretical contour plots is the delineation of a zone of downwarping to the west of the profile line. One possible explanation for the occurrence of this area is that it is associated with the seismic activity along the seismically mapped down step of the main fault plane (Whitcomb et al., 1973). A significant amount of left lateral motion on a steeply dipping plane could produce the localized downward displacements that are observed in this area. The addition of this fault geometry was not considered in this study, however.

4.6 Resolvability of Features in the Slip Model.

The variance operator, **V**, for this case is a 47 x 47 matrix. This matrix was calculated in the same manner in the previous chapter. For simplicity, the splay fault elements were suppressed in these resolvability calculations. This suppression should cause no change in the

conclusions reached in this section. Again, to test the resolvability of a particular feature of a model, a model perturbation affecting this feature will be considered. This perturbation will then be tested for detectability at the 95% confidence level.

The initial model that we consider is that shown in Figure 4.5. The first question that we ask about this slip model is the following: "Considering that the fault geometry of this model is appropriate, do the data demand that there exists a sharp minimum in the slip in the upper 1 km of the fault sheet?" To answer this question, we assume a perturbation, which when added to the calculated slip model, will just cancel this minimum. This perturbation is then tested and uniformly reduced until it is at the 95% confidence limit detectability threshold. The resulting perturbation is shown in Figure 4.13a. We see that the maximum perturbation allowable by the data is not large enough to erase this minimum.

Next, we try to determine if the data demand the existence of the broad minimum in slip between the upper and lower parts of the thrust sheet. Figure 4.13b shows the amount of slip that could be added in this region. We see here that the slip gradient could be smaller than that given in the original slip model, but nevertheless, the

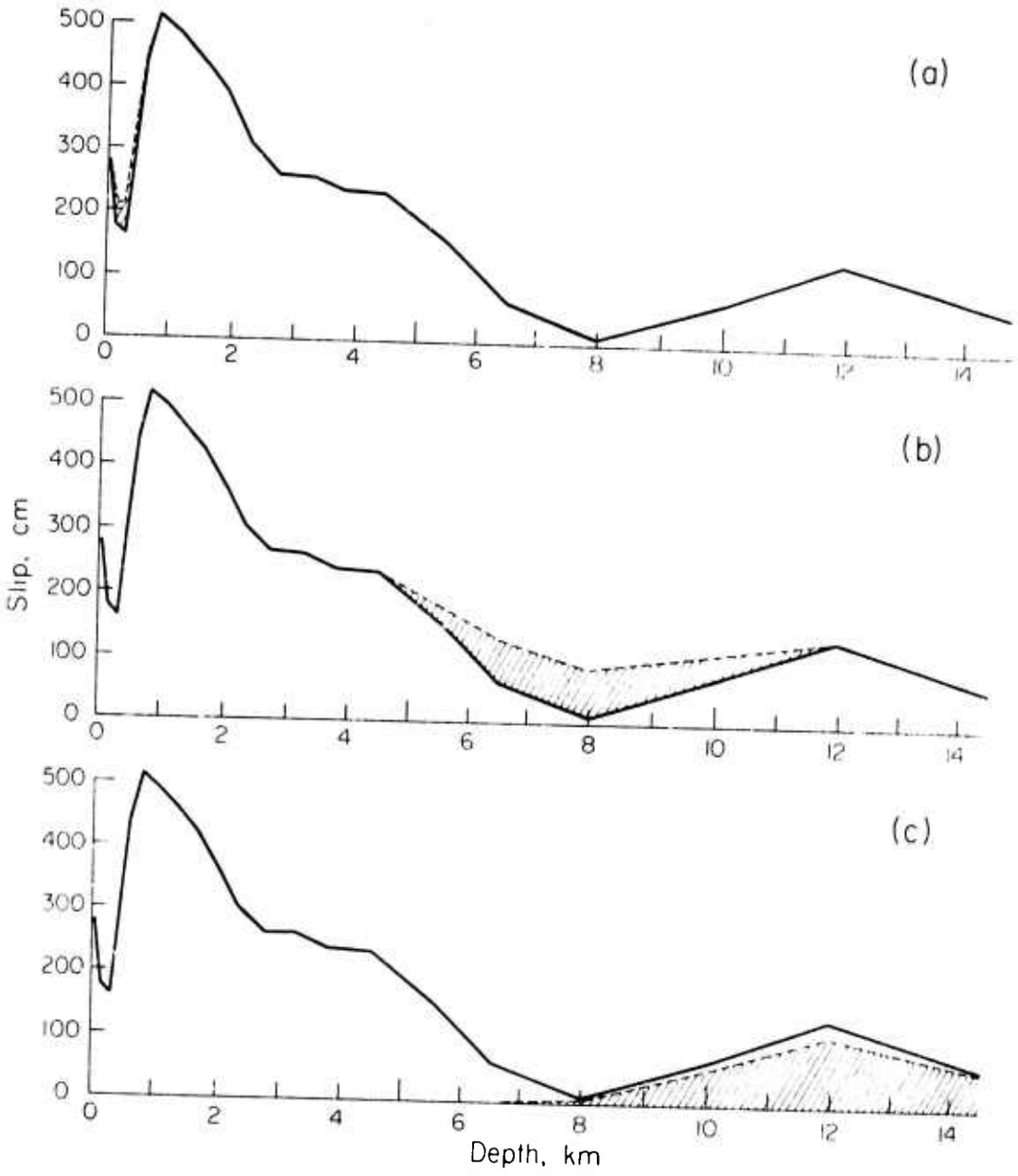

Figure 4.13. Examples of the resolvability of features of the best fit model solution given in Figure 4.5.

dislocation does become smaller with increasing depth in this region.

Intuitively, we would expect that the resolvability would be less in the hypocentral area than in other parts of the fault system because the fault elements in this region are located farther from the points on the surface where we have data. Also the density of data points on the surface near the epicenter is smaller than near the surface ruptures and the data in this area are generally not as accurate. In testing the resolvability of the calculated dislocation in the hypocentral area, we will consider what is the maximum perturbation that we can subtract from the calculated values and still be resolvable by the data. From equation (2.33) we see that the sign of the perturbation to be tested by our resolvability criterion is not important, only the magnitude of the perturbation. Thus, we can either add or subtract a perturbation tested at a particular confidence level to the calculated model dislocation and still not be detected by the data at that confidence level. In Figure 4.13c, we see that we can add or subtract about 100 cm of displacement in the hypocentral region for this perturbation shape. From this type of analysis, we indeed find that the slip in the hypocenter is poorly determined, since the uncertainty in slip is almost the equivalent of the calculated

values. If required to give bounds for the slip in this area as predicted by the static data used here, we would say that the maximum slip is approximately 130 cm ± 100 cm.

We now consider the variance operator in which the San Gabriel fault representation is included in the fault geometry, but the splay system is still excluded. The slip model for which perturbations are considered is that given in Figures 4.7 and 4.8. Figure 4.14 shows these perturbations. In the upper part of this figure, we see that considering displacement on the San Gabriel fault alone, that is, not taking into account any coupling between fault elements, there would be about a 100 cm uncertainty in the estimate of the slip. The lower part of this figure shows the maximum undetectable perturbation possible when slip on this auxiliary fault and slip in the hypocentral region are considered simultaneously. We see here that the uncertainty in slip in the hypocentral area is almost the same as that in Figure 4.13c, while the uncertainty on the San Gabriel fault has been reduced to about 50 cm.

4.7 Averaging Operators.

As discussed in the previous chapter, examination of the kernels of the matrix operator, **R**, provides information about the filter through which we are able to view our "best fit" estimate of the fault slip. We say that the

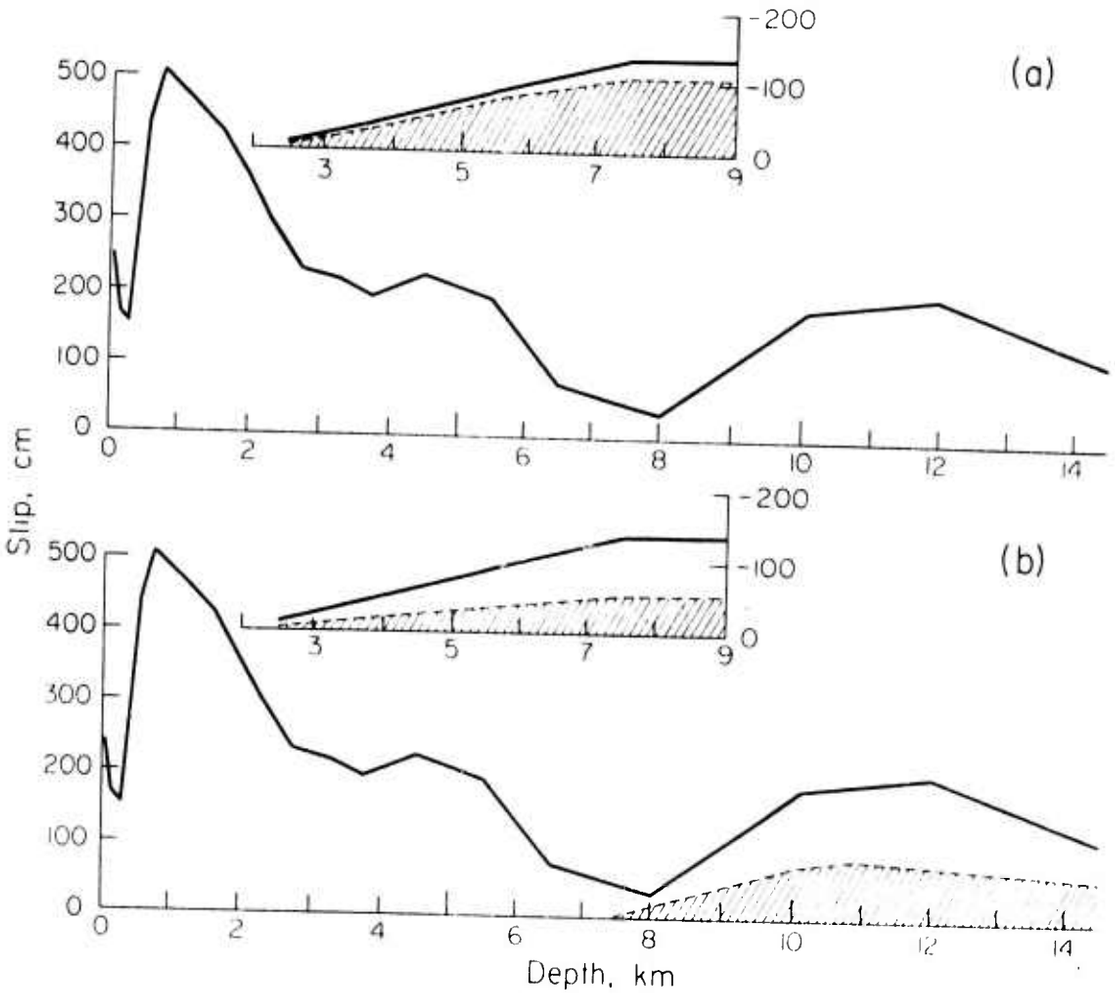

Figure 4.14. Examples of the resolvability of features of the best fit model solution given in Figures 4.7 and 4.8.

ability to resolve the details of the actual dislocation function depends on the size of the kernels and the averaging widths of the kernels. The ratio of the size of the kernels to the averaging widths provides a convenient medium for expressing the resolution at a given point in the fault system. First of all in this section, we would like to examine these ratios to determine the effect of the addition of the gravity-converted displacement points to the data set. The averaging operator was calculated both with and without these data points in the inversion data set and the averaging ratios calculated in both instances.

Figure 4.15 shows the difference in the averaging ratios the addition of this data causes. The fault geometry considered in this case is that of a single thrust sheet. In the figure, we see that the upper part of the fault is unaffected by the addition of this data. The area of the fault which has the maximum effect is in the range from 7-11 km depth. In this range, the resolvability ratio is doubled. The reason for the increase is not so much an increase in the value of the averaging kernels for these elements, but more so the fact that the averaging widths of these elements are reduced. Thus, the addition of these data does not help much in the determination of the actual

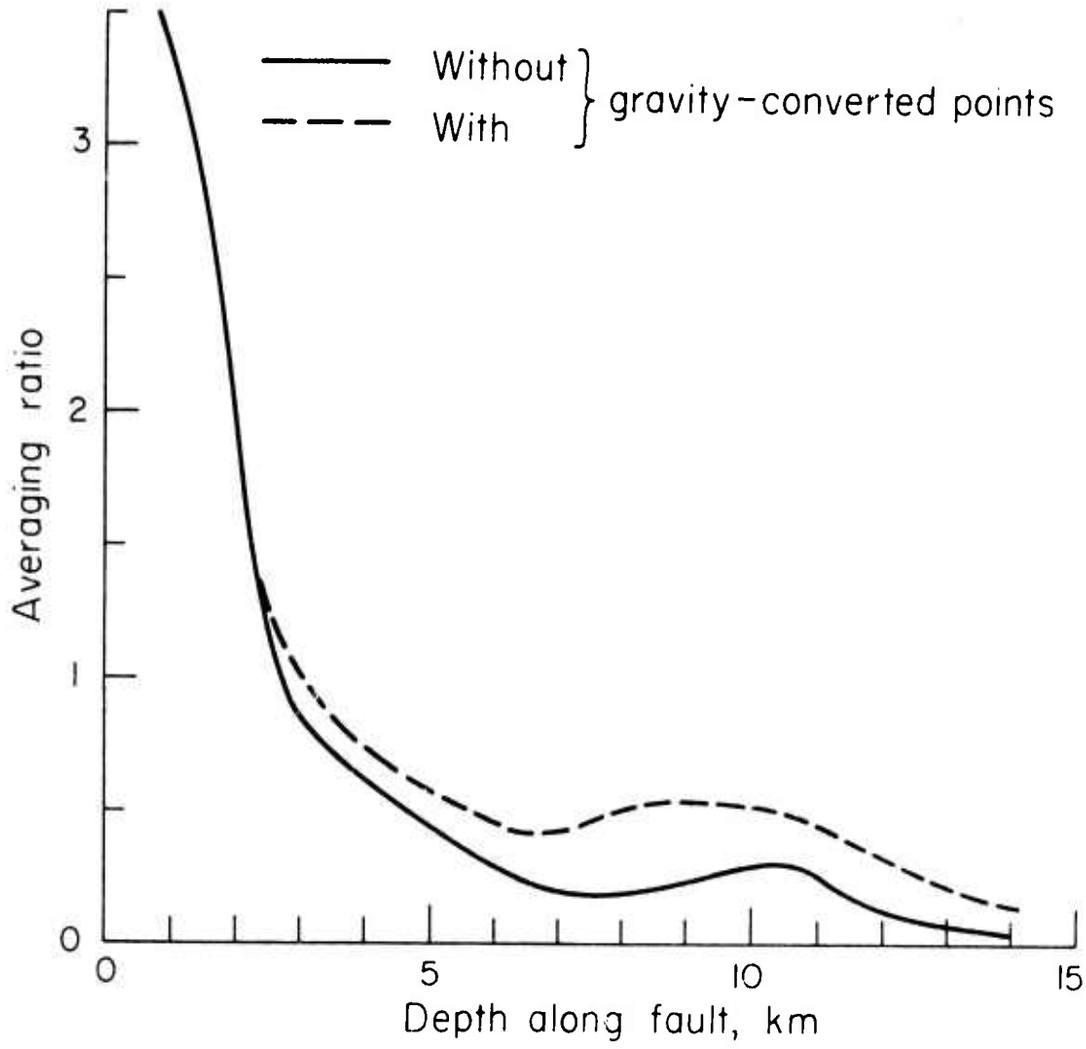

Figure 4.15. Averaging ratios for data sets with and without the gravity-converted displacement data. Curve has been made continuous by connecting values calculated at the fault element mid-point depths.

slip in this area, but the slip that is determined is much more localized than could be determined without these data.

Figure 4.16 shows examples of the averaging kernels for the San Fernando earthquake model consisting of a simple thrust sheet. The arrows in the figure indicate the elements around which the averaging is centered. The block offset to the right is an expanded view of the upper 1.5 km of the cross section to elucidate the fault geometry in that area. Examining this figure, we see that the averaging is very localized in the upper part of the fault, but the averaging length increases with increasing depth along the fault. In the bottom figure, the averaging length (half-width) is about 4.5 km. In comparing the averaging kernels presented here with those given for the Alaska earthquake, we notice that the strong negative side lobes are not as in evidence in this present example. This is probably caused by the better spatial distribution of data in the San Fernando case.

Figure 4.17 indicates the averaging kernels for selected fault elements when the San Gabriel fault geometry is introduced. The top figure is centered on a fault element that is located on the main thrust sheet directly under the San Gabriel fault representation. We see from this picture that there is no coupling in this area between

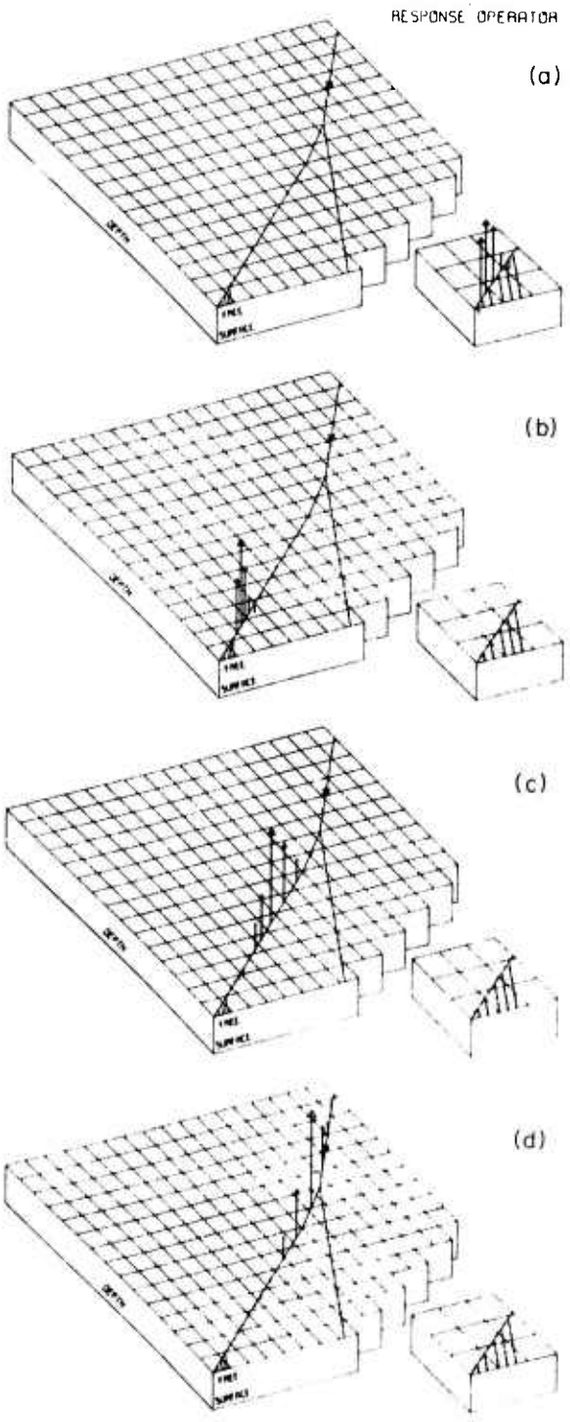

Figure 4.16. Spatial averaging of slip on the single thrust sheet model.

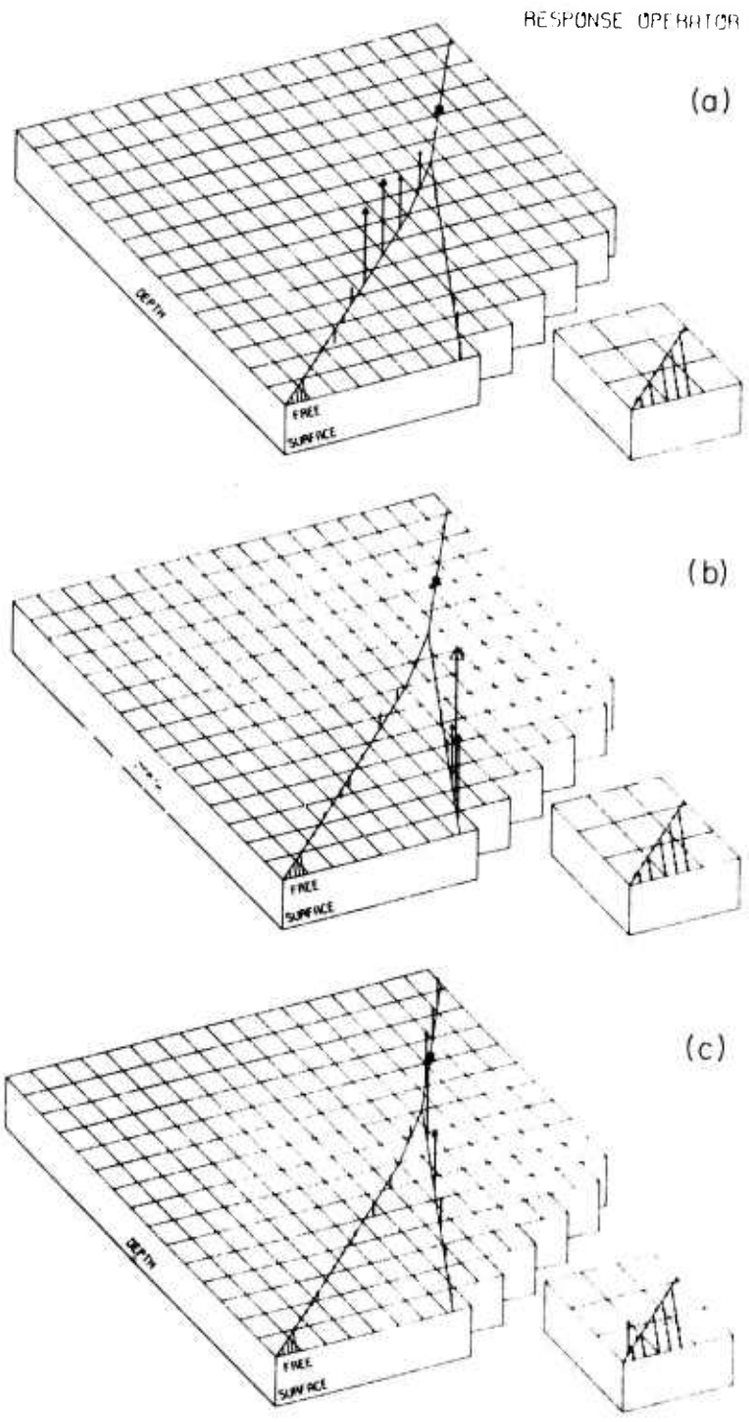

Figure 4.17. Spatial averaging of slip in model with San Gabriel fault representation.

the main fault and the auxiliary fault. This means that there can be no trade-off in displacement between the two faults to affect the resolvability test of the slip in this area as indicated in Figure 4.13b. Figure 4.17b shows the spatial averaging of slip for the upper part of the San Gabriel fault. We see here that this too is uncoupled from the rest of the fault system. We note here that the best fit solution for the fault geometry which included this fault indicated little or no slip on this portion of the fault. Figure 4.17c indicates the extent of the spatial averaging for the lower part of the San Gabriel fault. We see here that there is very strong coupling to the fault elements in the hypocentral area. We note that the averaging between the two fault segments is in the same direction indicating that any normal slip on this portion of the San Gabriel fault will be seen by the data as normal slip averaged over both the San Gabriel fault and the main fault in the hypocentral area. However, we can rule out the possibility of the occurrence of normal faulting on the main fault from consideration of the focal mechanism of the initial motion. These observations are taken to mean that this portion of the San Gabriel fault is effectively decoupled from the rest of the fault system. If this is true, then from the results indicated by the resolvability calculations in Figure 4.14a, the slip on this fault is not

detectable by the data. This conclusion is not surprising considering that we have presented two separate dislocation models -- one without slip on the San Gabriel fault (Figure 4.5) and one with slip on the San Gabriel fault (Figure 4.7) -- each of which is geophysically plausible and fits the data to a satisfactory degree.

4.8 Conclusions.

Several possible fault dislocation models have been presented to explain the observed vertical displacement which accompanied the 1971 San Fernando, California earthquake. The fault geometry assumed in calculating these models was made to conform to most of the geological and geophysical observations that were associated with the faulting. In each of the models computed from the inversion scheme, a significant variation in slip along the fault was calculated. The maximum displacement was computed to have occurred on the shallow end of the fault surface. The resolution of slip in this shallow part was very good, and the spatial averaging of slip was relatively small. A model was calculated in which there was extensive splaying away from the main fault as the fault neared the surface. The slip model calculated for this geometry is preferable to that of a single fault for the following two reasons: 1) The maximum displacement on the fault necessary to fit the data was reduced, and large variations in slip in

the upper 1 km of section was reduced; and 2) evidence for the existence of and movement on these splay faults was observed in the field, and their existence admits the possibility of modeling the observed lateral offset in the surface faulting. We caution here that the exact number, location and offset on the splay elements should not be taken as absolute. The addition of these elements into the fault system was taken to represent in some systematic fashion the observable imbricate ruptures which did not appear to be so systematic. However, we think that the inclusion of these elements has led to a better understanding of the faulting process near the surface.

Dislocation models were calculated for fault geometries which both included and excluded a representation of the San Gabriel fault. It was found that there was very little resolution of slip along the San Gabriel fault. If slip did occur, this slip would be normal fault movement and confined to the lower part of the fault. These two models indicated that between 140 and 200 cm of slip occurred in the area of initial motion. The uncertainty of this slip in the hypocentral area as determined by the static data is about 100 cm. All of these calculations have been based on the initial assumption that the fault sizes were fixed. If we have misjudged the length of the

fault elements, the calculated slip would be in slight error. For distances away from the fault elements, this error is about linear with length. That is, if the lengths of the fault elements in the hypocentral area are actually 10% smaller than the value that was fixed in the inversion, the calculated slip on the smaller fault element would be about 10% larger.

The moment for this event can now be calculated for each of the slip models. In the calculations, the value of the shear modulus was taken from the estimates given by Jungels (1973, p. 29). The values of moment range from 1.0 x 10^{26} dyne-cm for the slip model presenting in Figure 4.5 to 2.2 x 10^{26} dyne-cm for the model given in Figure 4.10. These two extremes just about span the values obtained by both static and dynamic observations given in the literature by various authors (Aki, 1971; Wyss, 1971; Wyss and Hanks, 1972; Canitez and Toksöz, 1972; Jungels and Frazier, 1973; Savage et al., 1973).

On the basis of choosing the simplest possible model necessary to fit the data, we give as our preferred "best fit" model the slip function given in Figure 4.5 with the addition of the splay slip shown in Figures 4.10 and 4.11.

Appendix 2

Observed Gravity Changes Associated with Deformation Accompanying the 1971 San Fernando Earthquake

A2.1 Introduction

In the past there have been a limited number of studies of gravity changes which accompany earthquakes. The earliest of these studies were in Japan. Tsuboi et al. (1953) attempted to compare changes in gravity and precise line leveling changes following the Nankaido earthquake of 1946. However, a significant comparison could not be made due to the imprecise gravity values. Extensive gravity surveys in the area of the Matsushiro earthquake swarms of 1965-1968 were carried out by Harada (1968). A comparison of this data to the leveling resurvey associated with the earthquake swarms by Tsubokawa et al. (1967) has been reported by Kasahara (1970) and Hagiwara and Tajima (1973). In this study, the relation between the gravity change and the vertical upward displacement associated with the tectonic deformation of the earthquake swarms nearly coincided with a Bouguer gradient with a density taken to be 1.0 gram/cm^3. The maximum displacements that were observed where the gravity field was being monitored were just over 30 cm and the maximum gravity changes were about 0.06 mgal with an accuracy of $\pm$ 0.02 mgal. However, during the

period of ground subsidence the changes in the gravity field appeared to fall along the free-air gradient. As a whole the swarm process left no effective gravity change, even though the residual displacement was about 20 cm.

Barnes (1966) and Rice (1969) conducted remeasurements of gravity in an area affected by the deformation of the Alaska, 1964, earthquake. The changes in gravity were compared with changes in elevation determined by a post-earthquake releveling of a 1923 first-order geodetic line coincident with the gravity traverse. Because the area in which the traverse was located had a maximum elevation change of only 0.6 m, the relationship between gravity and elevation changes could not be determined accurately. However, the largest gravity differences indicated that the slope of the Δg-ΔE relationship was closer to the Bouguer gradient with a density of 2.67 gram/cm^3 than to the free air gradient.

Hunt (1970) has observed a relation between changes in the gravity field and elevation changes for the 1968 Anangahua earthquake. Although his data is meager, the gradient of Δg-ΔE relation between -0.15 and -0.20 mgal/m is much less than the free air gradient -0.309 mgal/m.

In each of these cited studies, the conclusions reached by the researchers were limited by either the inability to accurately measure the vertical component of

displacement or accurately determine changes in the gravity field at points where elevation changes are known. Thus in order to establish a meaningful correlation of deformation and accompanying gravity changes, the vertical displacements need to be large and accurately known, and reliable gravity stations need to have been established in the area prior to the earthquake. The calibration, stability and sensitivity of gravity meters are sufficient now to make gravity measurements for reliable studies. Once the correlation between ΔE and Δg has been established then the gravity meter could be used as a reconnaissance tool to map the extent of deformation rapidly following a large earthquake if previous gravity stations have been established.

Much of the tectonic deformation due to the 1971, San Fernando, California, earthquake fortunately occurred in an area in which there was a dense leveling net and enough reoccupiable gravity stations that a study could be carried out. The gravity stations in the San Fernando Valley were installed as part of a survey by Corbató (1963) using a Worden gravimeter (W88) and very tight control on the observed gravity values. Most of the stations described by Corbató were actually installed in 1958. These stations were reoccupied and the results are reported here. A compilation of all the observed gravity changes in the

area affected by this earthquake is given by Oliver et al. (1973). This study includes data in both the San Fernando Valey and the San Gabriel Mountains, both south and east of the epicenter and northwest of the earthquake area.

A2.2 Gravimeter Characteristics

All gravity measurements employed in this study were made with a Worden Master (W533) gravimeter. The small dial constant of this meter as determined from the tilt table method at the manufacturer (Texas Instruments) in 1968 was 0.33181 mgals per large scale division when the instrument is operating at 87°F. Most of the measurements taken in this study were taken when the internal temperature of the meter was between 70°F and 72°F. Since the response of the instrument is linear in this temperature range, a simple extrapolation gives the dial constant at 72°F to be 0.33145 mgals per large scale division. In addition, the meter was checked on a previously established seven station calibration loop between a station located at the University of California at Los Angeles (UCLA) and Mt. Wilson. The gravity station at the California Institute of Technology (Caltech) is the second station in this loop -- denoted MW2. This calibration loop was established by Harrison and Corbató (1965) using a LaCoste and Romberg geodetic gravimeter. Further discussions and descriptions of this loop can be found in Biehler (1964) and Robbins

et al. (1973). The total gravity change from MW2 to the station at Mt. Wilson is 323.80 mgals. Successive checks of the instrument over this loop yielded a calibration value of 0.3315 ± 0.0002 mgals per large scale division. With careful measurements and averaging values, instrument readings at individual stations are reproducible to within 0.1 large scale division, or 0.03 mgals. In the actual survey, readings at individual stations were tied to the base station by closed loops, with several readings being made at each of the individual stations.

The instrument drift due to tides, small temperature changes, internal fatigue, etc. varied somewhat but never seemed to exceed 0.15 mgals per hour. The instrument drift was linearly interpolated in time throughout the closure of each individual loop.

A2.3 Base Station Ties

All the reoccupation readings were based on ties to the base station at Caltech. The gravity station at Caltech, MW2, used here should not be confused with another close-by station described by Chapman (1966, p. 25, No. 309). A description of the location of this and all other stations referred to in this chapter is given by Robbins et al. (1973). Individual reoccupation stations were tied to the base station on at least four to five separate occasions, and it is thought that the maximum error of each

tied station is about ± 0.03 mgals based on the standard deviations of the scatter in the data about the mean values. Two of the reoccupation stations tied to the base station were checked with a LaCoste-Romberg gravimeter, with a calibration constant of about 0.1 mgals per large scale division, and the differences in the gravity readings between the two stations and the base station determined with this instrument agreed to within ± 0.01 mgal (Oliver, person communication, 1971).

Since the original gravity stations installed by Corbató were based on direct ties to the gravity station at UCLA and the reoccupation of these stations were based on ties to Caltech, the question arises as to whether or not there was a relative change between Caltech and UCLA caused by the earthquake, or whether or not the absolute gravity changed at both of these stations. Oliver et al. (1973) reported that there was indeed no gravity change at Caltech within the reliability of 5 pre-earthquake and 6 post-earthquake measurements made relative to UCLA or to a station at Menlo Park, California. Supplementary evidence for this conclusion comes from the fact that a continuously recording tidal gravimeter operating at UCLA at this time of the earthquake indicated no perceptible change in the gravity field at that point relative to the accuracy of that instrument (±0.001 mgal). In addition, the Mt. Wilson

calibration loop was rechecked relative to a distant calibration loop, and no changes in the gravity values could be observed. Thus, we feel relatively comfortable in basing our reoccupation readings on ties to the gravity station at Caltech.

A2.4 Gravity Station Reoccupation.

Figure A2.1 shows the location and distribution of the reoccupied gravity stations in the San Fernando Valley. The stations are identified with a number corresponding to that given by Corbató (1963). The stations numbered 1-14 were the sub-base stations of Corbató's net and are well scattered throughout the San Fernando Valley. These sub-base stations were the first to be reoccupied, since immediately following the earthquake, before any precision leveling could be done, the areal extent of the tectonic deformation was sought. It was assumed that the deformation, if any, would be reflected into changes in gravity. The absolute gravity at these sub-base stations was more accurately determined than at the other stations, with the values generally known to within $\pm$ 0.03 mgals. Of the fourteen stations originally comprising the sub-base net, eleven could be recovered in 1971, although there was some slight uncertainty as to the exact location of three of the stations. These uncertain stations are marked with an asterisk in Table A2.1. At these uncertain stations, an

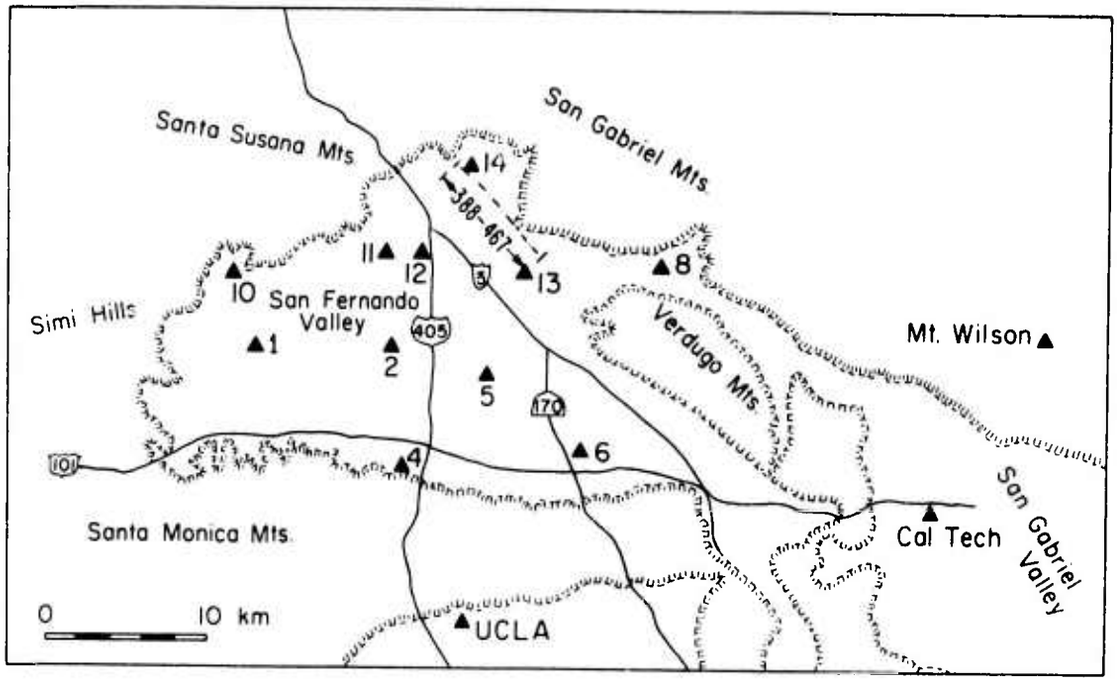

Figure A2.1. Index map of the San Fernando Valley showing the location of the reoccupied gravity stations.

TABLE A2.1

Stn. No.	Pre-1971 Gravity (mgals)	σ_{g_1} (mgals)	Post-Earthquake Gravity (mgals)	σ_{g_2} (mgals)	Δ_g (mgals)	σ_g (mgals)	ΔE (m)	σ_E (m)
1	567.35	.03	567.39	.03	0.04	.04	-	-
2	563.19	.03	563.20	.03	0.01	.04	-0.03	.03
4	589.34	.03	589.34	.08	0.00	.09	-	-
5	567.78	.03	567.75	.05	0.03	.06	-	-
6	579.19	.03	579.16	.03	-0.03	.04	-	-
8*	537.25	.03	537.09	.05	-0.16	.06	-	-
10	571.25	.03	571.25	.03	0.00	.04	-	-
11*	536.43	.03	536.23	.05	-0.20	.06	-	-
12	539.70	.03	539.55	.03	-0.15	.04	0.00	.03
13*	547.01	.03	546.98	.03	-0.03	.04	-	-
14	526.02	.03	525.72	.03	-0.30	.04	1.35	.05
388	543.97	.05	543.99	.03	0.02	.06	-0.05	.03
393	534.83	.05	534.78	.03	-0.05	.06	0.01	.03
444	530.38	.05	530.28	.03	-0.10	.06	0.25	.12
446	527.52	.05	527.40	.03	-0.12	.06	0.16	.03
448	525.03	.05	524.71	.03	-0.32	.06	1.47	.03
449	527.62	.05	527.57	.03	-0.05	.06	0.32	.03
458	523.38	.05	523.17	.03	-0.21	.06	1.17	.06
459	519.73	.05	519.54	.03	-0.19	.06	0.98	.05
460	515.30	.05	515.20	.03	-0.10	.06	0.58	.03
461	507.17	.05	507.08	.03	-0.09	.06	0.48	.03
464	521.28	.05	521.16	.03	-0.12	.06	0.82	.03
467	518.28	.05	518.20	.03	-0.08	.06	0.50	.03

Table A2.1. Observed gravity and elevation changes.

attempt was made to take the readings at about the same altitude as reported by Corbató (1963). The gravity values for all the stations for both the pre-earthquake and post-earthquake measurements are listed here. The absolute gravity values are the values listed plus 979.0 gals. The values given by Corbató (1963, Appendix B) are the pre-earthquake values rounded to the nearest 0.1 mgal. However, the values were actually calculated to the nearest 0.01 mgal (Corbató, personal communication, 1971). The uncertainties, σ_{g_1}, σ_{g_2}, are based on standard deviations about the mean values. The uncertainty of the resulting change in gravity, σ_g, is given by the square root of the sum of the squares of the standard deviations of the two measurements. The change in gravity, Δg, is defined to be the post-earthquake measurement minus the pre-earthquake measurement.

In the last two columns, the changes in elevation, ΔE, and their respective standard deviations for the stations, σ_E, are given when available. These values were obtained principally from the City of Los Angeles, Bureau of Engineering, Van Nuys Office. The measurements of elevation both before and after the earthquake are made relative to the mean tidal level in the City of San Pedro, California. Since most of the Corbató gravity stations were located on, or very near, city engineering monuments, this data was very useful. Supplementary leveling information from

Burford et al. (1971) was used. The estimated variance in the leveling data is from these sources. With the exception of two points, the changes in the leveling data are relative to the elevation determined in 1960. These two exceptions are Station 2 and Station 12 which are relative to measurements in 1970 and 1963 respectively. Station 12 is especially anomalous in that in the period 1963-1970 the elevation increased by 0.06 m, but between 1970 and post-earthquake 1971, the elevation decreased by 0.06 m.

From the upper part of this table, it is seen that the only significant changes in gravity occurred to the north of the observed surface ruptures, with the exception of Station 12, which is discussed below. Twelve more stations all concentrated above, or slightly below, the rupture zone were then reoccupied. The gravity values measured at these stations are listed in the lower half of Table A2.1.

A2.5 Relation of Gravity Differences to Observed Deformation.

The gravity stations listed in the lower half of Table A2.1 form a profile from the southeast to the northwest cutting across the main surface ruptures. The location of this profile in relation to the surface deformation can be seen in Figure A2.4. Figure A2.2 shows the results of the reoccupation of the stations along this profile. The top part of the figure gives the observed elevation change from 1960 to 1971 showing the sharp scarp where the profile

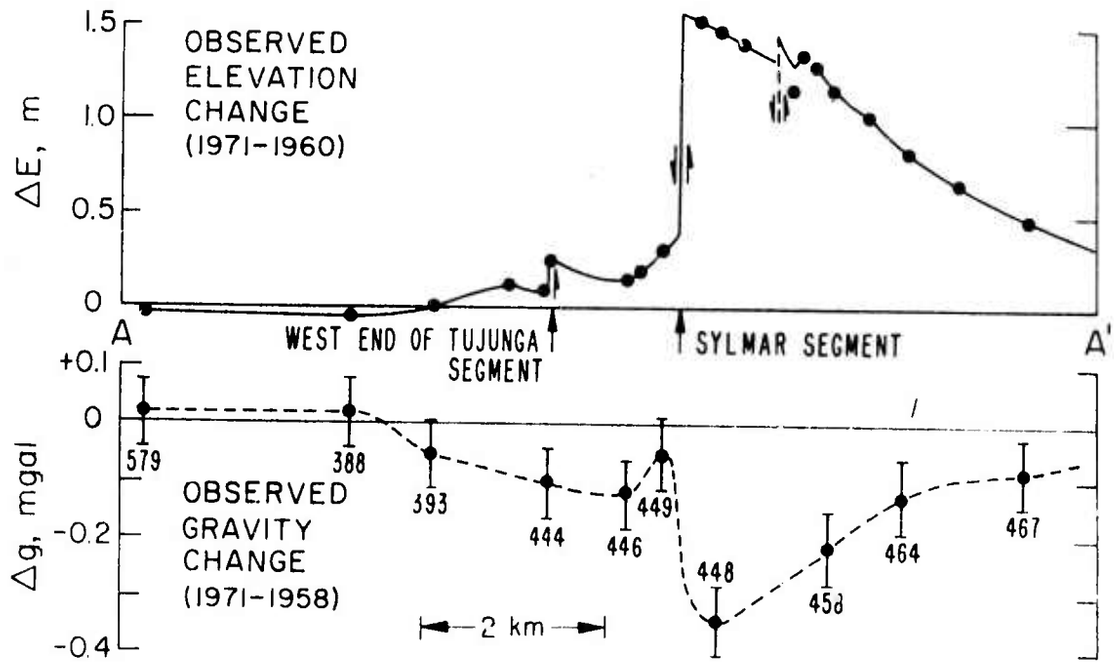

Figure A2.2. Gravity profile A-A' showing the relation of the changes in surface elevation to gravity changes.

crosses the Sylmar segment of the surface breaks. The profile crosses just at the western end of the Tujunga segment of the surface breaks. The lower part of the figure indicates the corresponding observed gravity change for this profile. It is clear that a good relationship exists between the observed elevation change and the observed gravity change. Now if we plot the significant changes in gravity versus their respective changes in elevation, we see that the relation is quite linear. Figure A2.3 shows this plot. The line fit to the data is a least squares relation given by

$$\Delta g = - 0.215\ \Delta E \pm 0.026 \qquad \text{(A2.1)}$$

where ΔE is the elevation change in meters and Δg is the gravity change in mgals. The gradient of this relation implies a Bouguer reduction density of 2.2 gram/cm^3, or about the density of the unsaturated surficial layers in the area, which are late Cenezoic sediments. If a Bouguer reduction density of 0.2 gram/cm^3 higher or lower than this value is chosen, the fit is only slightly degraded, with the standard error being increased. As an example, a gradient of - 0.224 mgals per meter is found when a Bouguer reduction density of 2.0 gram/cm^3 is used. The gradient for the relation for the interval of acceptable Bouguer

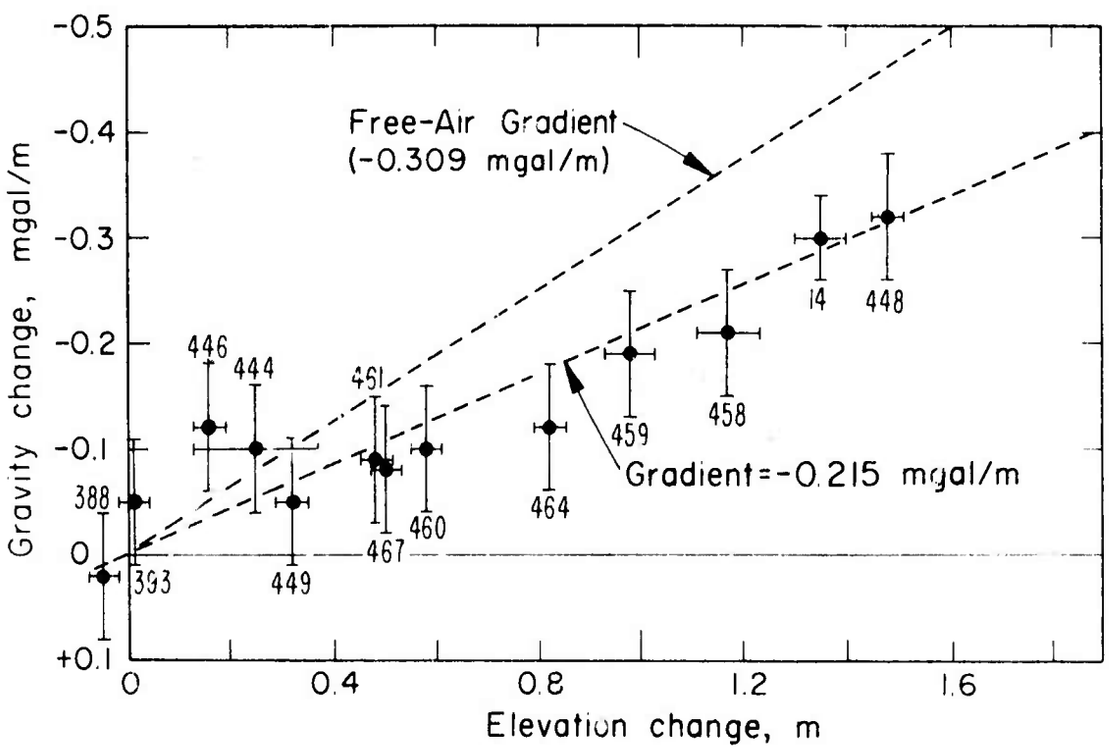

Figure A2.3. Least-squares fit of elevation changes to the gravity changes. The uncertainties in the measurements are indicated by the error bars for each numbered station. Points fall along a gradient significantly less than the free-air gradient.

reduction density values is still significantly less than the free air gradient of - 0.309 mgals per meter.

If the deformation as measured along this profile had occurred as the result of merely a vertical expansion over some depth, then the gravity changes would have fallen along the free air gradient. However, the fact that the values fall along a reasonable Bouguer reduction gradient indicate that by some means mass was added beneath the gravity stations. Within the resolving power of the gravity measurements, one can conclude that the overriding thrust block appeared to move as a unit. For the regions of uplift, it is clear that these areas of negative gravity change are now slightly heavier than before the earthquake due to the added mass from the stacking of the surficial layers on the pre-earthquake surface.

Equation A2.1 can be inverted to give the estimated elevation change for a known gravity change. This relation is

$$\Delta E = -4.65 \, (\Delta g + \sigma_g) \, . \qquad (A2.2)$$

Equation A2.2 implies that if the gravity changes at the stations reoccupied can be determined to $\pm$ 0.05 mgals, then the accompanying change in elevation is determined to $\pm$ 0.23 m.

The gravity change data accumulated in this study has been added to that obtained by the other authors in Oliver et al. (1973) to give a contour map of the gravity changes associated with this earthquake (Figures A2.4). Releveling data from both that obtained from the City of Los Angeles Engineering Bureau and that obtained by the U. S. Geological Survey, as reported in Burford et al. (1971) has been converted into changes in gravity and included into the gravity contours shown in this figure. The gravity changes that are obtained by conversion of leveling data are shown in parentheses along side the bench mark location and the year that the original elevation was obtained. Gravity data obtained directly are similarly shown without the parentheses. Examination of the two sets of data show that they are remarkably compatible within the uncertainties of each of the data sets. Of particular interest is a comparison of the gravity values from both data sets in the area just east of the Pacoima Reservoir. The gravity change from the converted elevation change (-0.15 mgals) is based on a 1929 elevation determination, where the direct gravity changes are based on measurements obtained in 1964 and 1970, yet the change based on the 1929 observation is about the same size as those based on much later observations. Savage et al. (1973) have postulated that this particular releveling datum might contain some pre-earthquake secular

Reproduced from best available copy.

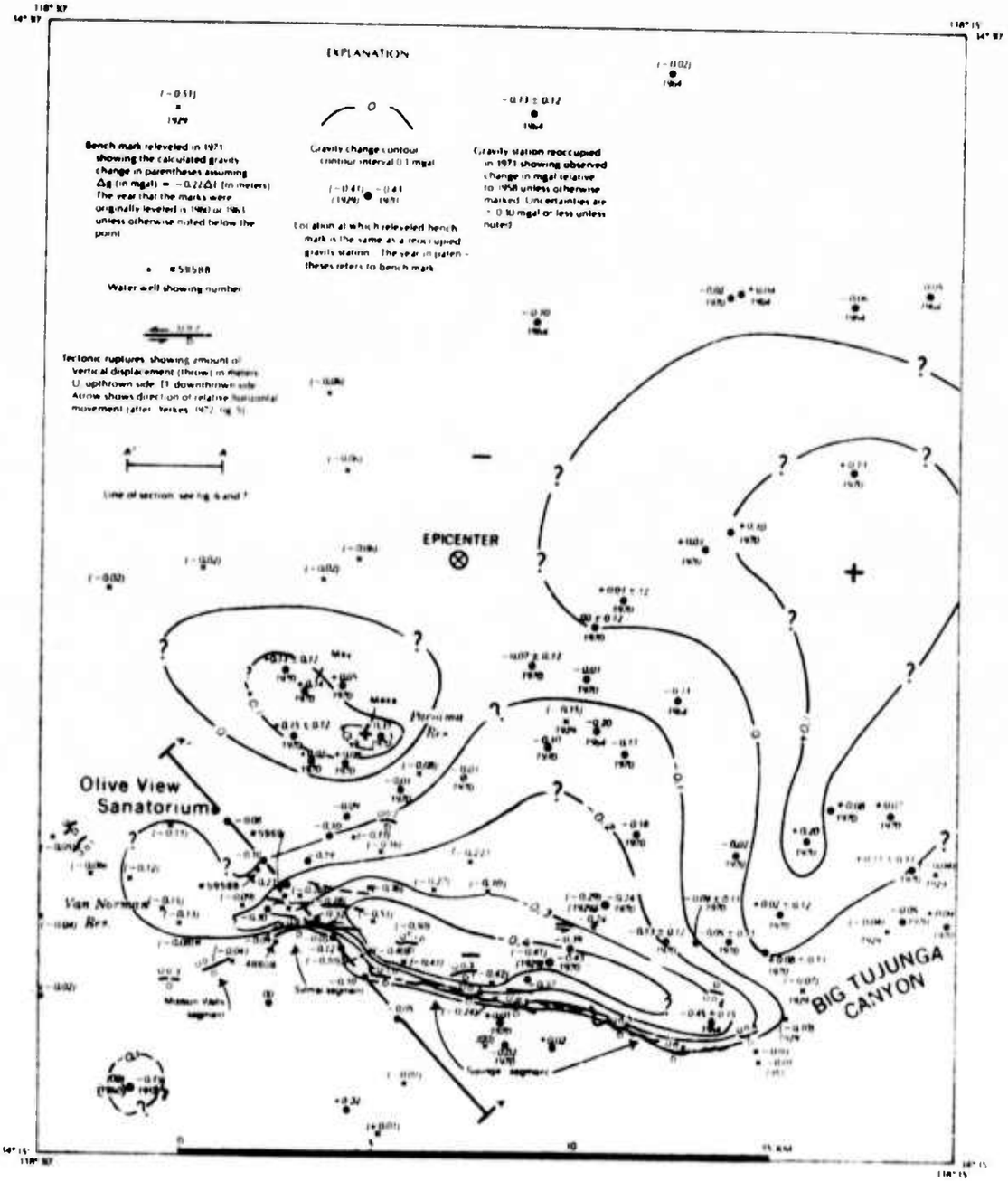

Figure A2.4. Contour map of the gravity changes associated with this earthquake. This data includes elevation changes that have been converted to gravity changes by equation (A2.1).

uplift, however, the gravity measurements here suggest that most of the uplift in this area probably took place at the time of the earthquake and was not distributed in the 42 years preceding the earthquake.

Also indicated in Figure A2.4 are areas of positive gravity changes, indicating subsidence. These areas were not delineated by the leveling surveys because of lack of data. Although the data indicating these positive changes are less accurate than in this study, the majority of the points defining the positive change do have positive values when the maximum error is subtracted. If these gravity changes obey a similar Bouguer relationship with changes in elevation, then this is an indication that mass was removed from this area. No attempt has been made to balance the mass involved because of the poor nature of some of the data. However, the recognizance of this area of subsidence shows the usefulness and facility of making gravity measurements in tectonic areas whether or not they can be done in conjunction with leveling surveys. It is interesting to note that this area roughly forms an inverted "U" and corresponds to about the aftershock zone near the epicentral area (Allen et al., 1971).

A2.6 Bouguer Residuals.

Figure A2.5 shows the residual Bouguer anomaly for the profile A-A'. This residual was calculated from the formula,

$$\delta g_{BA} = \Delta g - 0.215\ \Delta F \ . \qquad \text{(A2.3)}$$

The residuals are plotted in the upper part of Figure A2.5. Although the residuals are fairly small when compared to the estimated errors for each observation, the calculated anomalies are systematic in the sense that the residuals are negative south of the surface ruptures and positive to the north of the surface ruptures. Although barely significant, these anomalies represent some rearrangement of the subsurface mass from 1958 to 1971. One obvious rearrangement of the subsurface mass is that which can be caused by the raising or lowering of the areal water table in the time interval between gravity measurements. Oliver et al. (1973) have considered this in some detail. They report that for the limited water table level data that is available for this area, the water table level changed in the short interval about the time of the earthquake only by the amount the surface was deformed. Thus the entire sedimentary unit sampled by the water wells moved as a unit during the earthquake. However, in the 13-year interval, 1958 to

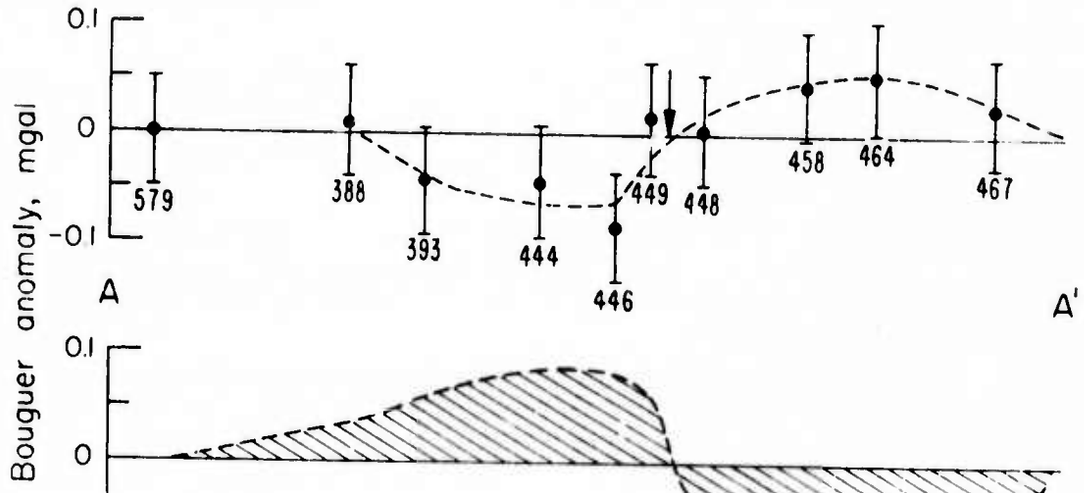

Figure A2.5. Upper--Observed Bouguer residuals for the gravity profile A-A'. Lower--Calculated gravity effects from the fluctuation in the water-table level, 1958-1971, for this profile.

1971, the total water table level, after seasonal effects are removed, was lowered in the area north of the surface ruptures and actually raised in the area to the south of the surface ruptures. Oliver (1972, personal communication) has calculated the gravitational effects of this net change in the water table level and his results for the profile A-A' are plotted in the lower half of Figure A2.5.

It is seen here that the water table effects give rise to about the size gravity anomaly as that observed, however, it is in the opposite direction. That is, the water table effect must be subtracted from the observed Bouguer anomaly to get the corrected total Bouguer anomaly. The errors in the gravity changes associated with the water table fluctuations are at least as large as the errors in the upper part of Figure A2.5 based on the uncertainty and paucity of the input data. It is not wished to emphasize this anomaly too much, other than perhaps the general form of the anomaly. No attempt was made in this study to model the anomaly, since not much is known about the original density distribution of the subsurface.

A2.7 Discussion.

The reoccupation of gravity stations after a major earthquake is shown to be a rapid and relatively inexpensive method of delineating the areas of deformation caused by the earthquake, provided a detailed gravity net is

established prior to the occurrence of such an event.

The occurrence of the San Fernando earthquake in an area where there was such good control on the elevation and gravity changes has presented the best opportunity to establish an accurate relation between these two variables for this particular type of faulting. A gravity station reoccupation traverse across the zone of the maximum thrust fault surface ruptures yielded a propertionality between the observed gravity changes and changes in elevation. The slope of the relationship shows rather convincingly that the elevation changes and the gravity changes are not related simply by the free air correction, but rather along a Bouguer gradient. The Bouguer reduction density found by a least-squares fit to the data indicates that the greatest portion of the gravity change could be explained by the stacking of the surficial layers on the pre-earthquake surface. In retrospect, this is exactly what would be expected from reverse thrust faulting. The Bouguers anomalies derived for this profile, although statistically barely significant, are systematic in that they are generally positive to the north of the rupture zone and negative to the south of the rupture zone.